

國立交通大學
材料科學與工程學系
博士論文

鐵-9wt.%鋁-28wt.%錳-1.8wt.%碳合金顯微
結構、機械性質及抗腐蝕性質研究

Microstructures, Mechanical Properties and Corrosion
Resistance in an Fe-9wt.%Al-28wt.%Mn-1.8wt.%C Alloy

研究生：張凱明

指導教授：劉增豐 博士

朝春光 博士

中華民國一百零三年七月

Microstructures, Mechanical Properties and Corrosion Resistance in an Fe-9wt.%Al-28wt.%Mn-1.8wt.%C Alloy

研究生：張凱明

Student: Kai-Ming Chang

指導教授：劉增豐 博士

Advisor: Dr. Tzeng-Feng Liu

朝春光 博士

Dr. Chuen-Guang Chao

國立交通大學
材料科學與工程學系
博士論文

A Dissertation

Submitted to Department of Materials Science and Engineering

College of Engineering

National Chiao Tung University

in Partial Fulfillment of the Requirements

for the Degree of

Doctor of Philosophy

in

Materials Science and Engineering

July 2014

Hsinchu, Taiwan, Republic of China

中華民國一百零三年七月

誌 謝

感謝指導教授劉增豐教授與朝春光教授教導，使學生能夠順利完成此論文。感謝莊振益教授在研究論文上指導。感謝師母林美慧老師鼓勵與關心，對於學生能完成學業有莫大的影響。學生在此致上最誠摯的感謝。

口試時承蒙郭金國教授、吳忠春教授等口試委員悉心指正，學生由衷感謝。

感謝實驗室夥伴們的幫助，學長王承順博士、蘇俊瑋博士、段逸軒博士、蔡國棟博士、林志龍博士、楊小姐及學弟陳柏至博士、浩仰、永昌、育誠、明翰還有其他眾多曾經在鐵鋁錳實驗室的同學及林耀楠博士、祥溢、Bill 在交大認識的好友，在此致上最深的感謝。特別感謝亦師亦友的林耀楠博士、林志龍博士、祥溢及 Bill，因為你們讓我在研究之路充滿歡樂與正向力量。

感謝家人的愛，讓美夢成真。讓我在過程中瞭解愛的真諦。得之於人太多，出之於己太少。謝謝愛我的父母和岳父母、姑姑錦華、妹妹志佳、兒子善詠、太太欣怡。

感謝在這過成中幫助過我的所有人與力量，謝謝您們。

2014/07/29

交大後山

鐵-9wt.%鋁-28wt.%錳-1.8wt.%碳合金顯微

結構、機械性質及抗腐蝕性質研究

研究生：張凱明

指導教授：劉增豐 博士

朝春光 博士

國立交通大學材料科學與工程研究所

中文摘要

本論文利用穿透式電子顯微鏡，掃描式電子顯微鏡，X-光能量散佈分析儀，LECO 2000 影像分析儀與 Instron 拉伸試驗機研究觀察 Fe-9wt.%Al-28wt.%Mn-1.8wt.%C 合金顯微結構與機械性質之關係。並研究離子氮化對表面硬度和抗腐蝕性質影響。依據實驗的結果，本論文所得到的具體研究結果如下：

(一)、在淬火狀態下，Fe-9wt.%Al-28wt.%Mn-1.8wt.%C 合金的顯微結構是沃斯田鐵相(Austenite, γ)，且在沃斯田鐵基地內具有高密度、細微奈米級的 κ' -碳化物，此奈米級 κ' -碳化物是在淬火過程中藉由史賓諾多分解 (spinodal decomposition) 反應所產生的。此 κ' -碳化物的形成機構與過去學者在時效處理後的鐵-(7-10)wt.%鋁-(28-32)wt.%錳-(0.54-1.3)wt.%碳 ($C \leq 1.3$ wt.%) 合金中發現的細微 κ' -碳化物截然不同。在

$C \leq 1.3\text{wt.}\%$ 的 Fe-Al-Mn-C 合金中，淬火狀態下為單一沃斯田鐵相， κ' -碳化物只能在時效後才能產生。由於 Fe-9wt.%Al-28wt.%Mn-1.8wt.%C 合金在淬火狀態下，沃斯田鐵基地內就具有高密度、細微奈米級的 κ' -碳化物存在，所以其最大拉伸強度(ultimate tensile strength (UTS))、降伏強度(yield strength (YS))與延伸率(E1)分別可達到 1080 MPa、868 MPa 和 55.5%。因此 Fe-9wt.%Al-28wt.%Mn-1.8wt.%C 合金在淬火狀態下之機械性質明顯的優於其它學者所研究的 $C \leq 1.3\text{wt.}\%$ 的鐵錳鋁碳合金在淬火狀態時之機械性質。因為 Fe-9wt.%Al-28wt.%Mn-1.8wt.%C 合金在淬火狀態下即具有 κ' -碳化物，所以在達到最佳的強度與延性組合的機械性質所需的溫度與時間均可大幅減少。將淬火合金在 450°C，時效 12 小時，可得到最佳強度和延性組合，其最大拉伸強度、降伏強度與延伸率分別可達到 1552 MPa、1423 MPa 和 25.8%。

(二)、Fe-9wt.%Al-28wt.%Mn-1.8wt.%C 合金的淬火結構為沃斯田鐵相 (austenite, γ)，且在 γ 基地內有十分緻密奈米級(nano-sized)的 $(\text{Fe, Mn})_3\text{AlC}$ 碳化物(κ' -碳化物)。緻密奈米級的 κ' -碳化物是合金在固溶化淬火過程中藉由史賓諾多分解(spinodal decomposition)相變化在 γ 基地內形成。將在淬火狀態下的 Fe-9wt.%Al-28wt.%Mn-1.8wt.%C 合金，經 450°C、12 小時、壓力範圍 133-798 Pa 離子氮化處理後，在 γ 基地內的 κ' -碳化物會成長且量變多，而使氮化後合金能具有優異的強

度和延性組合，且隨著氣體壓力的增加在合金表面分別可得到 6~15 μm 厚的氮化層，此氮化層結構由 X-繞射可知，主要組成為具有面心立方 (Face-Centered Cubic, FCC) 型之 B1-AlN 及少量的 FCC γ' -Fe₄N；藉由離子氮化處理後的 Fe-9wt.%Al-28wt.%Mn-1.8wt.%C 合金表面硬度可高達 1710 Hv，基材硬度為 540 Hv，且在 3.5%鹽水中具有極佳抗腐蝕性質，這些特性都遠優於一般經最佳氮化處理後的高強度合金鋼，工具鋼，麻田散鐵不銹鋼及析出硬化型不銹鋼。



Microstructures, Mechanical Properties and Corrosion Resistance in an Fe-9wt.%Al-28wt.%Mn- 1.8wt.%C Alloy

Student: Kai-Ming Chang

Advisor: Dr.Tzeng-Feng Liu

Dr. Chuen-Guang Chao

**Department of Materials Science and Engineering
National Chao Tung University**

Abstract

The relationships between microstructures and tensile properties of an Fe-9wt.%Al-28wt.%Mn-1.8wt.%C alloy have been examined by transmission electron microscopy, scanning electron microscopy, energy-dispersive X-ray spectrometry, LECO 2000 image analyzer and Instron tensile testing machine, respectively. Microstructures, mechanical properties and corrosion behaviors of the plasma-nitrided Fe-9wt.%Al-28wt.%Mn-1.8wt.%C alloy have also been investigated. On the basis of the experimental examinations, the results can be summarized as follows :

[1] The as-quenched microstructure of the Fe-9wt.%Al-28wt.%Mn-1.8wt.%C alloy is

austenite phase containing a high density of extremely fine nano-sized κ' -carbides. The κ' -carbides were formed during quenching by spinodal decomposition. The unique κ' -carbides formation mechanism is quite different from that observed in the Fe-(7~10)wt.%Al-(28~32)wt.%

Mn-(0.54~1.3)wt.%C ($C \leq 1.3$ wt.%) alloys, in which the fine nano-sized κ' -carbides could only be observed in the aged alloys. Owing to the presence of the high density of the extremely fine κ' -carbides within the austenite matrix, the ultimate tensile strength (UTS), yield strength (YS) and elongation (El) of the as-quenched Fe-9wt.%Al-28wt.%Mn-1.8wt.%C alloy was 1080 MPa, 868 MPa and 55.5%, respectively. Evidently, the mechanical property of the as-quenched alloy is superior to that of the as-quenched FeMnAlC ($C \leq 1.3$ wt.%) alloy examined by previous workers. Since the κ' -carbides already exist in the as-quenched alloys, both the aging time and temperature for obtaining the optimal combination of strength and ductility can be significantly reduced. When the alloy was aged at 450°C for 12 hours, the ultimate tensile strength (UTS), yield strength (YS) and elongation (El) of the Fe-9wt.%Al-28wt.%Mn-1.8wt.%C alloy was 1552 MPa, 1423 MPa and 25.8%, respectively.

[2] The as-quenched microstructure of the Fe-9wt.%Al-28wt.%Mn-1.8wt.%C alloy was austenite (γ) phase containing an extremely high density of nano-sized $(\text{Fe,Mn})_3\text{AlC}$ carbides (κ' -carbide). These κ' -carbides were formed within the austenite matrix by spinodal decomposition during quenching. The size and the amount of the κ' -carbides increased dramatically when the as-quenched Fe-

9wt.%Al-28wt.%Mn-1.8wt.%C alloy was plasma-nitrided at 450°C for 12h under nitriding pressures ranging from 133-798 Pa. Consequently, the nitrided alloys could obtain an excellent combination of strength and ductility after being plasma-nitrided. The thickness of the nitrided layers obtained are 6, 9 and 15 μm -thick under pressure of 133, 399 and 798 Pa, respectively. The nitride layer is composed predominantly of FCC B1-AlN with a small amount of γ' -Fe₄N. Due to the surface nitrogen concentration reached up to 18.4wt.% (44.3at.%), the surface hardness (1710 Hv), substrate hardness (540 Hv), and corrosion resistance in 3.5% NaCl solution of the plasma-nitrided Fe-9wt.%Al-28wt.%Mn-1.8wt.%C alloys are far superior to those obtained previously in optimally nitrided high-strength alloy steels, as well as martensitic and precipitation-hardening stainless steels.

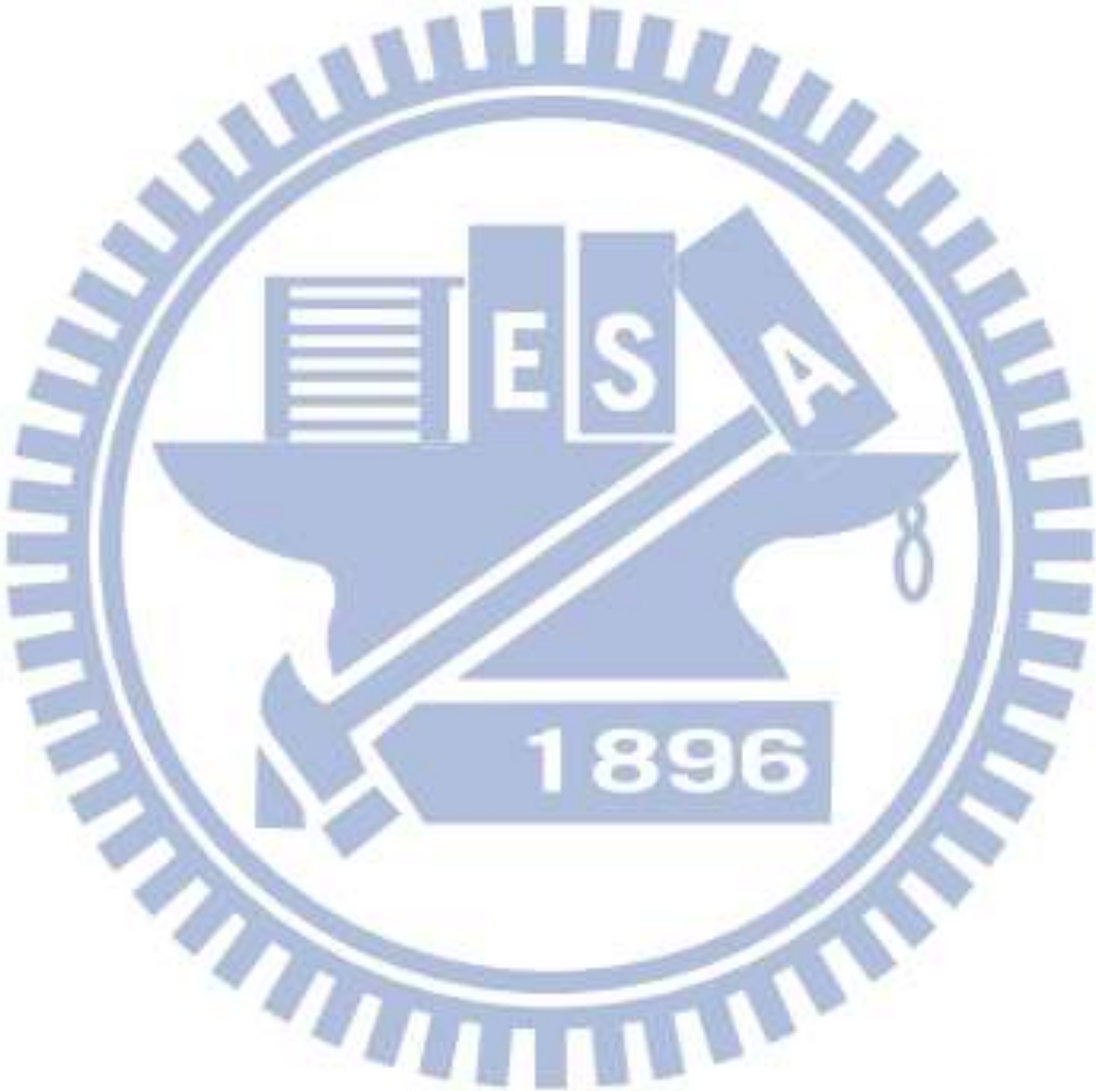
Contents

中文摘要	i
英文摘要(Abstract)	iii
Contents	vi
List of Tables.....	vii
List of Figures.....	ix
Chapter 1. General Introduction	1
References.....	8
Chapter 2. A novel high-strength high-ductility and high corrosion-resistance FeAlMnC low-density alloy	12
2-1 Introduction.....	14
2-2 Experimental Procedure.....	16
2-3 Results and Discussion.....	17
2-4 Conclusions.....	21
References.....	22
Chapter 3. Structure and properties of gas-nitrided nanostructured Fe-9Al- 28Mn-1.8C alloy	32
3-1 Introduction.....	34
3-2 Experimental Procedure.....	38
3-3 Results and Discussion.....	40

3-4 Conclusions49

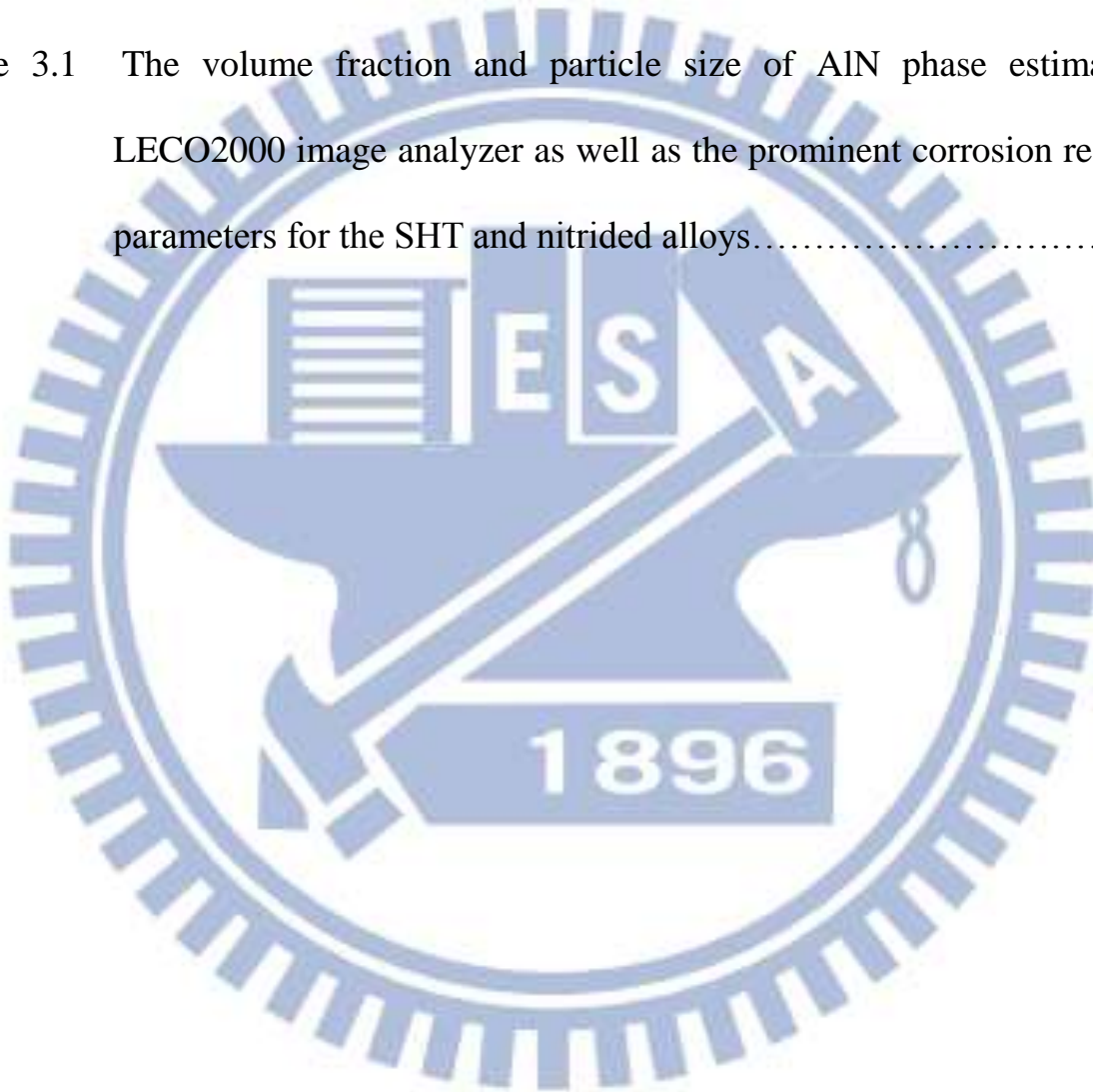
References50

List of Publications63



List of Tables

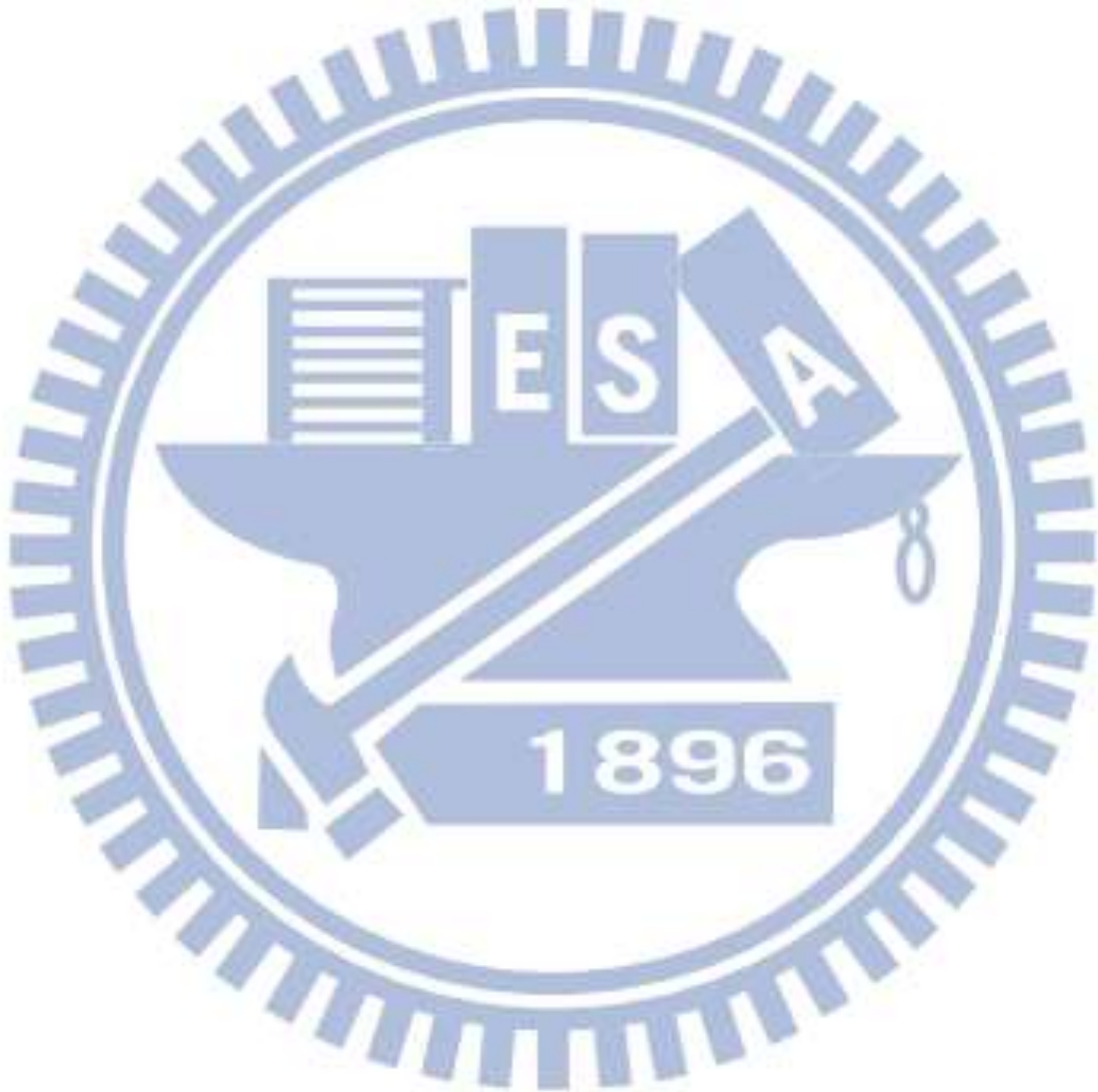
Table 2.1	Tensile properties of the alloy in the as-quenched condition and aged at 450°C for various times.	31
Table 3.1	The volume fraction and particle size of AlN phase estimated by LECO2000 image analyzer as well as the prominent corrosion resistance parameters for the SHT and nitrided alloys.....	62

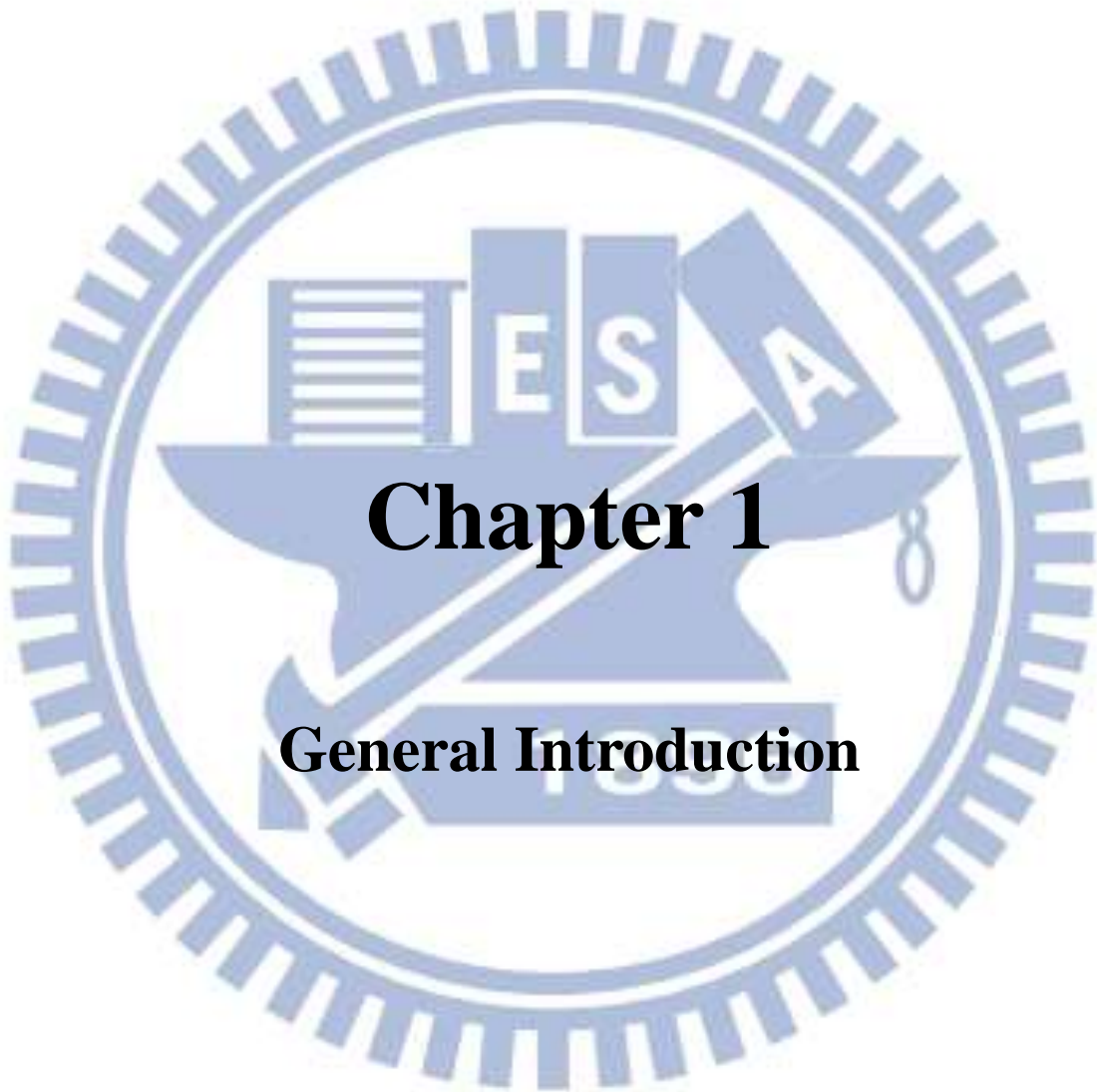


List of Figures

- Figure 2.1 Transmission electron micrographs of the as-quenched alloy: (a) bright-field image, (b) a selected-area diffraction pattern taken from the mixed region of austenite matrix and fine κ' carbides. The foil normal is $[001]$ (hkl : γ matrix; hkl : κ' -carbide), and (c) $(100)_{\kappa'}$ dark-field image.....24
- Figure 2.2 Scanning electron micrographs of the alloy aged at 450°C for (a) 9 h, (b) 12 h, and (c) 15 h, respectively.....26
- Figure 2.3 Scanning electron micrographs taken from the tensile fracture surface and free surface, respectively, of the specimen aged at 450°C for (a)-(b) 9 h, (c)-(d) 12 h, and (e)-(f) 15h.28
- Figure 3.1 SEM images of the present nitrided alloys treated with nitriding pressure of (a) 133 Pa, (b) 399 Pa, and (c) 798 Pa, respectively. (Etched in 5 % nital .)54
- Figure 3.2 XRD results for the untreated and nitrided alloys.....56
- Figure 3.3 (a) Nitrogen concentration, and (b) hardness profiles as a function of the depth for the present nitrided alloys treated with nitriding pressure of 133 Pa, 399 Pa and 798Pa, respectively.....57
- Figure 3.4 SEM images of the surface of nitrided alloys treated with nitriding pressure of (a) 133 Pa, (b) 399 Pa, and (c) 798 Pa, respectively.....58
- Figure 3.5 (a) Polarization curves for the untreated and nitrided alloys in 3.5% NaCl

solution. (b)-(d) : SEM images of the polarized alloys, (b) untreated alloy, (c-d) nitrided alloys with nitriding pressure of 133 Pa and 798 Pa, respectively.....60





Chapter 1

General Introduction

General Introduction

Austenitic FeAlMnC alloys have been subjected to extensive researches over the last several decades, because of their promising application potential associated with the high mechanical strength and high ductility [1-29]. In the FeAlMnC alloy systems, both Mn and C are the austenite-stabilizing elements. The austenite (γ) phase has a face-centered-cubic (FCC) structure; while Al is the stabilizer of the ferrite (α) phase having a body-centered-cubic (BCC) structure. Hence, by properly adjusting the contents of the three alloying elements, it is possible to obtain fully austenitic FeAlMnC alloys at room temperature. Previous studies showed that the as-quenched microstructure of the Fe-(7-10)wt.%Al-(28-32) wt.%Mn-(0.54-1.3)wt.%C alloys was purely single γ -phase without any precipitates. Depending on the chemical composition, the ultimate tensile strength (UTS), yield strength (YS), and elongation of the as-quenched alloys were 840~993 MPa, 410~551 MPa, and 72-50%, respectively [30-38]. These results indicate that, although it is possible to obtain single γ -phase with excellent ductility in the as-quenched FeAlMnC ($C \leq 1.3$ wt.%) alloys by properly adjusting the alloy compositions, the mechanical strength of these alloys is relatively low. Thus, the as-quenched alloys are unable to achieve the goal of simultaneously possessing high mechanical strength and high ductility.

In order to improve the mechanical strength of the Fe-Al-Mn-C alloys, previous studies have revealed that when the as-quenched alloys were aged at 500-650 °C for moderate times, a high density of fine $(Fe,Mn)_3AlC$ carbides (so-called κ' -carbides)

was found to precipitate coherently within the austenite matrix. The κ' -carbide has an ordered face-centered-cubic (FCC) $L'1_2$ crystal structure [37-44]. From these previously extensive studies, the significant improvement of the mechanical strength obtained in the aged FeAlMnC ($C \leq 1.3\text{wt.}\%$) alloys is mainly due to the coherent precipitation of the fine κ' -carbides within the austenite matrix. However, since the κ' -carbides are rich in carbon and aluminum, the precipitation of these carbides from the supersaturated austenite matrix involves diffusion process of large amount of carbon and relevant alloying elements. Consequently, longer aging time and/or higher aging temperature are usually required. From numerous studies reported previously, an optimal combination of strength and ductility for the FeAlMnC ($C \leq 1.3\text{wt.}\%$) alloys could be obtained through aging treatment at 550 °C for 15~16 hours [37-40]. This is primarily because that under these treatment conditions, a tremendous amount of fine κ' -carbides was found to precipitate within the austenite matrix and no precipitates were formed on the grain boundaries. According to the previous studies, depending on the alloy compositions, the UTS, YS and El of the FeAlMnC ($C \leq 1.3\text{wt.}\%$) alloys aged at 550 °C for 15~16 hours can reach 1130~1220 MPa, 890~1080 MPa and 39~31.5%, respectively [37-40]. However, if the aging process was performed at 450 °C, it may take more than 500 hours to reach the same level of mechanical strength. Similarly, for 500 °C aging treatment, 50~100 hours were needed [37-40].

In another embodiment, previous studies also tried to prolong the aging time at

550~650 °C. However, it was found that prolonged aging not only resulted in the growth of the fine κ' -carbides but also led to the $\gamma \rightarrow \gamma_0 + \kappa$, $\gamma \rightarrow \alpha + \kappa$, $\gamma \rightarrow \kappa + \beta\text{-Mn}$, or $\gamma \rightarrow \alpha + \kappa + \beta\text{-Mn}$ reactions occurring on the grain boundaries [37-40, 45]. Where γ_0 is the carbon-depleted γ phase and the κ -carbides have the same ordered FCC $L'1_2$ structure as the κ' -carbide, except that they usually precipitate on the grain boundaries with larger size. [Note: Conventionally, for distinction purpose, the finer $(\text{Fe,Mn})_3\text{AlC}_x$ carbides formed within the austenite matrix are termed as “ κ' -carbides”, while the coarser $(\text{Fe,Mn})_3\text{AlC}_x$ carbides formed on the grain boundaries are termed as “ κ -carbides”]. As a result, prolonged aging treatments frequently resulted in embrittlement of the alloys due to the precipitation of coarse κ -carbides and $\beta\text{-Mn}$ precipitates on the grain boundaries [37-40, 44-46].

Recently, in order to further improve the strength, a small amount of V, Nb, Mo and W has been added to the austenitic FeAlMnC ($\text{C} \leq 1.3\text{wt.}\%$) alloys [47-50]. After solution heat-treatment or controlled-rolling followed by an optimum aging at 550°C for 16 hours, the UTS and YS of the FeAlMnMC ($\text{M}=\text{V, Nb, Mo, W}$) alloys could be noticeably increased up to 1130~1220MPa and 890~1080MPa, respectively, with 41~26% elongation [47-50].

Although the austenitic FeAlMnC alloys could possess excellent combination of strength and ductility, the corrosion behavior of the alloys in aqueous environments was not adequate for applications in aggressive environment [51-55]. In order to improve the corrosion resistance, Cr was added to the austenitic FeAlMnC alloys [54-

57]. Consequently, it was found that the corrosion potential (E_{corr}) and pitting potential (E_{pp}) of as-quenched austenitic Fe-(7.1-9.1)wt.%Al-(29.2-31.3)wt.%Mn-(2.8-6)wt.%Cr-(0.88-1.0)wt.%C alloys in 3.5% NaCl solution were ranging from -820 to -556 mV and from -240 to -27 mV, respectively [51-54]. The results were much better than the E_{corr} (-920~-789 mV) and E_{pp} (-500~-280 mV) of the as-quenched austenitic as-quenched FeAlMnC alloys [51-55].

FeAlMnC alloys could improve the corrosion resistance and maintain almost the same mechanical properties when Cr was added in the FeAlMnC alloys, however, it was not a cost-effective method. It is well-known that nitriding was widely utilized to improve surface hardness and corrosion resistance of high-strength steels. However, high-strength alloy steels, martensitic as well as precipitation-hardening stainless steels were needed to temper at 15 °C above the nitriding temperature prior to nitriding. Therefore, these high-strength alloy steels and stainless steels couldn't obtain remarkable combination of strength and ductility, as well as corrosion resistance, with the one-step treatment. It is worthwhile to explore how the corrosion behaviors and mechanical properties of the FeAlMnC alloys could be simultaneously optimized by one-step nitriding scheme for applications in aggressive environments.

The spinodal decomposition and formation of ordered κ' -particles were observed in the previous Fe-29wt.%Mn-9.8wt.%Al-(1.45-2.05)wt.%C alloys [58], under the as-quenched condition. In the FeAlMnC with C=1.35wt.% alloy, it was clearly seen that only diffraction peaks of austenite phase could be detected. This indicates that the as-quenched microstructure of the alloy with C=1.35wt.% is single austenite phase

without any κ' -carbides, which is similar to that found in the as-quenched austenitic FeAlMnC with $0.54 \leq C \leq 1.30$ wt.% alloys reported in the previous studies. However, when the carbon concentration was increased to above 1.45wt.%, an extremely high density of the nano-size (6~11nm) fine κ' -carbides with an $L'1_2$ crystal structure started to form within the austenite matrix. Furthermore, the sideband peaks around the $(200)_\gamma$ reflection could be observed in the alloys with $1.45 \leq C \leq 2.05$ wt.% alloys [58]. The presence of sidebands demonstrates that the ordered C-rich κ' -carbides and C-depleted γ_0 phase were formed through spinodal decomposition during quenching in the alloys with $1.45 \leq C \leq 2.05$ wt.%. Moreover, the intensity of the $(200)_{\kappa'}$ peaks increased with increasing carbon content, indicating that the amount of the nano-sized κ' -carbides increased with increasing carbon content. The existence of a high density of extremely fine κ' -carbides being formed within the austenite matrix through the spinodal decomposition mechanism during quenching is a novel feature. This novel feature has never been observed by the previous workers in the fully austenitic FeAlMnC ($0.54 \leq C \leq 1.30$ wt.%) alloys. However, the novel microstructures in the higher-carbon FeAlMnC alloys were previously studied principally by X-ray diffraction. Little transmission electron microscopy investigation concerning the microstructural information for the higher-carbon content FeAlMnC alloys has been provided. The experimental results evidently demonstrated that, due to the unique as-quenched microstructure of the present alloy, the effect of nitriding and aging could be achieved simultaneously with the one-step plasma nitriding

scheme. The main purposes of this study are described as follows :

(1) The first purpose is an attempt to investigate the microstructural developments of the Fe-9wt.%Al-28wt.%Mn-1.8wt.%C alloy in the as-quenched condition and aged at 450 °C for various times by using transmission electron microscopy, and to investigate the relationships between the microstructures and tensile properties.

(2) In order to achieve the effects of aging and nitriding simultaneously, the plasma nitriding treatments of the Fe-9wt.%Al-28wt.%Mn-1.8wt.%C alloy were fixed at 450 °C for 12h and the same gas composition with various nitriding pressures were used.

It is worth noting that, to date, little information concerning the effects of nitriding pressure on the structures and properties of the plasma nitrided Fe-Al-Mn-C alloys has been reported in the literature. The detailed experiment results are presented in Chapter 2 and Chapter 3, respectively.

References

- [1] T.F. Liu, C.M. Wan, Studies of Microstructures and Strength of Fe-Al-Mn Alloys, Proc. 7th Int. Conf. on the Strength of Metals and Alloys, Montreal, Canada, Aug. (1985) 423.
- [2] H. Ishii, K. Ohkubo, S. Miura, T. Mohri, Materials Transactions 44 (2003) 44 1679.
- [3] S.C. Mittal, R.C. Prasad, M.B. Deshmukh, Isij International 35 (1995) 302.
- [4] S. W. Lee, H. C. Lee, Materials Transactions 24 (1993) 1333.
- [5] Y.P. Chang, S.C. Lee, G.H. Tang, Journal of Materials Engineering and Performance 4 (1995) 627.
- [6] S.T. Chiou, W.C. Cheng, W.S. Lee, Mat Sci Eng A 386 (2004) 460.
- [7] S. T. Chiou, W. C. Cheng, W. S. Lee, Mat Sci Eng A 392 (2005) 156.
- [8] I.S. Kalashnikov, O Acselrad, L.C. Pereira, T. Kalichak, M.S. Khadyyev, J Mater. Eng. Perform. 9 (2000) 334.
- [9] S.C. Chang, W.H. Weng, H.C. Chen, S.J. Lin, P.C.K. Chung, Wear 181-183 (1995) 511.
- [10] W.T. Tsai, J.B. Duh, J.T. Lee, J. Mater. Sci. 22 (1987) 3517.
- [11] C.J. Wang, Y.C. Chang, Mater. Chem. Phy. 2002; 76: 151-161.
- [12] I.F. Tsu, T.P. Perng, Metall. Trans. A 22 (1991) 215.
- [13] S.M. Zhu, S.C. Tjong, Scripta 36 (1997) 317.
- [14] S.K. Banerji, Met. Prog. (1978) 59.
- [15] H.W. Leavenworth, Jr. and J.C. Benz, J. Met. (1985) 36.

- [16] J. Charles, A. Berghezan , A. Lutts, P.L. Dancoisne, *Met. Prog.* (1981) 71.
- [17] R. Wang, F.H. Beck, *Met. Prog.* (1983) 72.
- [18] J.C. Grcia, N. Rosas, R.J. Rioja, *Met. Prog.* (1982) 47.
- [19] D.J. Schmatz, *Trans. ASM.* 52 (1960) 898.
- [20] M.F. Alekseyenko, G.S. Krivonogov, L.G. Kozyreva, I.M. Kachanova, L.V. Arapova, *Met. Sci. Heat Treat.* 14 (3-4) (1972) 187.
- [21] L.I. Lysak, M.F. Alekseyenko, A.G. Drachinskaya, N.A. Storchak, G.S. Krivonogov, *Metallofizika.* 59 (4) (1975) 29.
- [22] R.E. Cairns, Jr. and J.L. Ham, U.S. Patent, No. 3111405 (1963).
- [23] I. Briggs, G.J. Russell, A.G. Clegg, *J. Mater. Sci.* 20 (1985) 668.
- [24] W.K. Choo, K.H. Han, *Metall. Trans. A.* 16 (1985) 5.
- [25] I. Gutierrez-Urrutia , *Scripta Metall.* 68 (2013) 343.
- [26] Editorial. *Scripta Metall.* 68 (2013) 337.
- [27] J. B. Seol, D. Raabe, P. Choi, H. S. Park, J.H. Kwakc, C. G. Parkb, *Scripta Metall.* 68 (2013) 348.
- [28] G.L. Kayak, *Met. Sci. Heat Treat.* 22 (2) (1969) 95.
- [29] Kim S.K., Choi J., Kang S. C., Shon I. R., Chin K. G. (2006), POSCO Technical Report, vol. 10, No.1, 106-114
- [30] S. M. Zhu, S. C. Tjong, *Metall. Mater. Trans. A* 29 (1998) 299.
- [31] C. N. Hwang, C. Y. Chao, T. F. Liu, *Scripta Matall.* 28 (1993) 263.
- [32] C. Y. Chao, C. N. Hwang, T. F. Liu, *Scripta Metall.* 28 (1993) 109.
- [33] S.C. Tjong, S.M. Zhu, *Mater. Trans.* 38 (1997) 112.

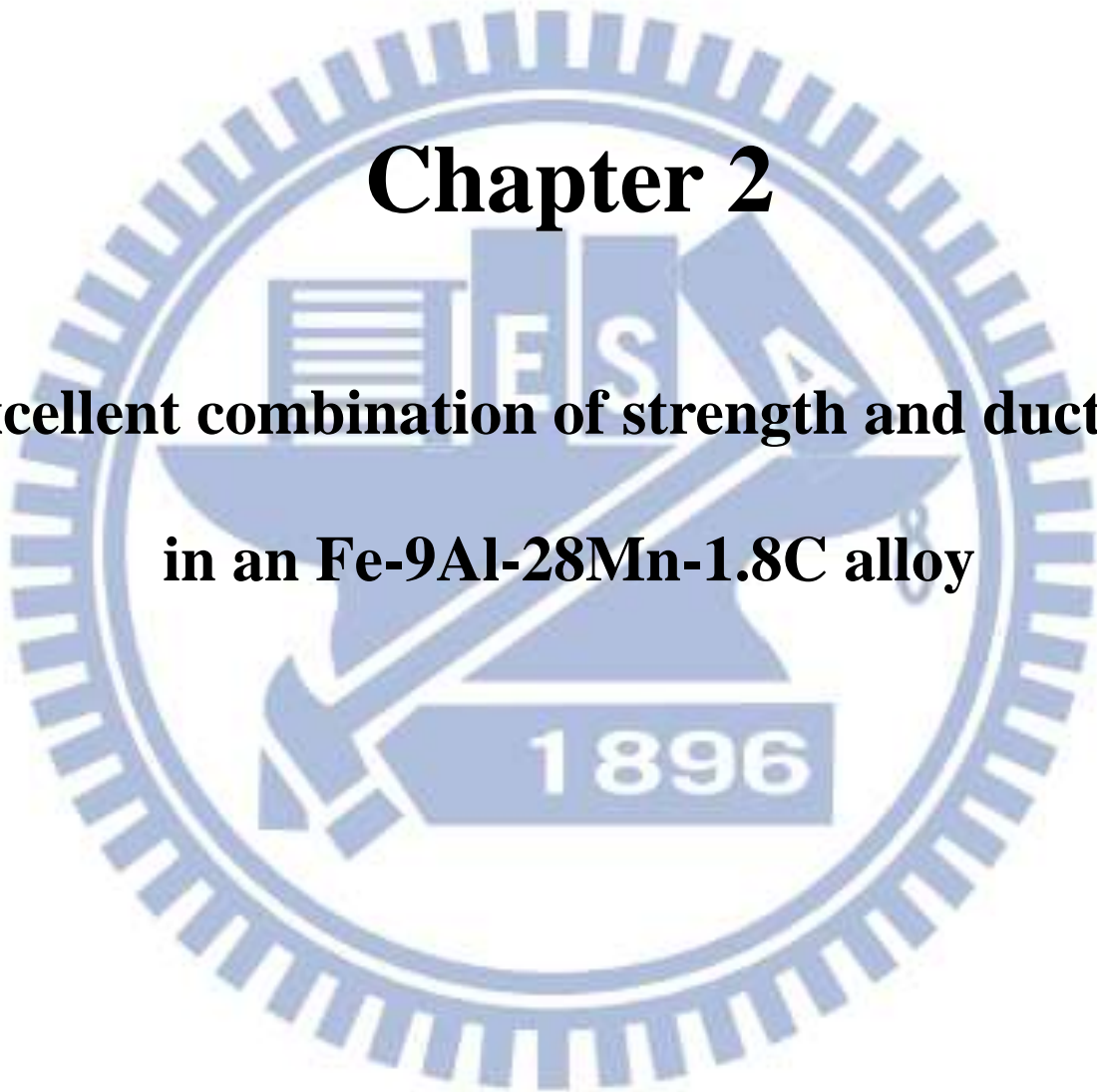
- [34] S.C. Chang, M. T. Jahn, J. Mater. Sci. 24 (1989) 1117.
- [35] H. J. Lai , C. M. Wan, J. Mater. Sci. 24 (1989) 2449.
- [36] E. K. James, Metall. Trans. A 19 (1988) 1873.
- [37] W. K. Choo, J. H. Kim, J. C. Yoon, Acta Mater. 45 (1997) 4877.
- [38] I. Kalashnikov, O. Acselrad, A. Shalkevich, L. C. Pereira, J. Mater. Eng.Perform. 9 (2000) 597.
- [39] K. T. Park, Scripta Mater. 68 (2013) 375.
- [40] I. Gutierrez-Urrutia, D. Raabe, Scripta Mater. 68 (2013) 343.
- [41] J. E. Krzanowski, Metall. Trans. A. 19 (1988) 1873.
- [42] K. Sato, K. Tagawa, Y. Inoue, Scr. Metall. 22 (1988) 899.
- [43] K. Sato, K. Tagawa, Y. Inoue, Mater. Sci. Eng. A. 111 (1989) 45.
- [44] K. Sato, K. Tagawa, Y. Inoue, Metall. Trans. A. 21 (1990) 5.
- [45] G. S. Krivonogov, M. F. Alekseyenko, G. G. Solov'yeva, Fiz. Metal. Metalloved. 39 (1975) 775.
- [46] S. C. Tjong, C. S. Wu, Mater. Sci. Eng. 80 (1986) 203.
- [47] G. S. Krivonogov, M. F. Alekseyenko, G. G. Solov'yeva, Fiz. Metall. Metalloved. 39 (1975) 775.
- [48] I. S. Kalashnikov, B. S. Ermakov, O. Aksel'rad, L. K. Pereira, Metall. Sci. Heat. Treat. 43 (2001) 493.
- [49] I. S. Kalashnikov, O. Acselrad, A. Shalkevich, L. D. Chumakova, L. C. Pereira, J. Mater. Process. Tech. 136 (2003) 72.
- [50] K. H. Han, Mater. Sci. Eng. A 279 (2000) 1.

- [51] M. Ruscak, T.P. Perng, Corrosion Oct. (1995) 738.
- [52] W.T. Tsai, J.B. Duh, J.T. Lee, J. Mater. Sci. 22 (1987) 3517.
- [53] J.B. Duh, W.T. Tsai, J.T. Lee, Corrosion Nov. (1988) 810.
- [54] S.C. Chang, J.Y. Liu, H.K. Juang, Corrosion 51 No.5 (1995) 399.
- [55] C.J. Wang, Y.C. Chang, Mater. Chem. Phys. 76 (2002) 151.
- [56] C.S. Wang, C.Y. Tsai, C.G. Chao, T.F. Liu, Mater. Trans. 48 (2007) 2973.
- [57] Y.H. Tuan, C.S. Wang, C.Y. Tsai, C.G. Chao, T.F. Liu, Mater. Chem. Phys. 114 (2009) 595.
- [58] G. D. Tsay, Y. H. Tuan, C. L. Lin, C. G. Chao, T. F. Liu, Mater. Trans. 52 (2011) 521.



Chapter 2

**Excellent combination of strength and ductility
in an Fe-9Al-28Mn-1.8C alloy**



Excellent combination of strength and ductility in an Fe-9Al-28Mn- 1.8C alloy

Abstract

An optimal aging at 450°C, the present alloy could possess a high yield strength 1383MPa with 32.5% elongation. With almost equivalent elongation, the yield strength was about 28% higher than that of FeAlMnC ($C \leq 1.3\text{wt.}\%$) alloys after solution heat-treatment or controlled-rolling followed by optimal aging. Additionally, due to pre-existing of fine $(\text{Fe,Mn})_3\text{AlC}$ carbides in as-quenched alloy, the aging time required for attaining the optimal combination of strength and ductility was much less than that of FeAlMnC ($C \leq 1.3\text{wt.}\%$) alloys.

2-1 Introduction

In previous studies, it is found that the as-quenched microstructure of the Fe-(7~10)wt.%Al-(28~32)wt.%Mn-(0.54~1.3)wt.%C alloys was single-phase austenite (γ) [1-9]. Depending on the chemical composition, the ultimate tensile strength (UTS), yield strength (YS) and elongation of the as-quenched alloys were 840~993MPa, 410~551MPa and 72~50%, respectively [5-8]. When the as-quenched alloy was aged at 550°C for about 16 h, a high density of fine (Fe,Mn)₃AlC carbides (κ' carbides) started to precipitate within the γ matrix and no precipitates were formed on the grain boundaries [8,9]. The resultant microstructure could possess the optimal combination of the mechanical strength and ductility. With an elongation better than about 30%, the values of 871~1259MPa for UTS and 665~1094MPa for YS could be attained [8,9]. Recently, in order to further improve the strength, a small amount of V, Nb, Mo and W has been added to the austenitic FeAlMnC ($C \leq 1.3$ wt.%) alloys [10-13]. After solution heat-treatment or controlled-rolling followed by an optimum aging at 550°C, the UTS and YS of the FeAlMnMC (M=V, Nb, Mo, W) alloys could be noticeably increased up to 1130~1220MPa and 890~1080MPa, respectively, with 41~26% elongation [10-13].

Additionally, the microstructural developments of the austenitic FeAlMnC alloys with higher carbon content have also been studied by several workers [14-16]. Interestingly, a high density of fine κ' carbides could be observed in the as-quenched Fe-(7.7~9)wt.%Al-(29~30)wt.%Mn-(1.5~2.5)wt.%C alloys [15,16]. The fine κ'

carbides were formed within the austenite matrix by spinodal decomposition during quenching [16]. This is different from that observed in the austenitic FeAlMn(M)C ($C \leq 1.3\text{wt.}\%$) alloys, in which the fine κ' carbides could only be observed in the aged alloys [1-9]. When the as-quenched alloy was aged at $550\text{-}800^\circ\text{C}$, the fine κ' carbides grew within the γ matrix and a $\gamma + \kappa' \rightarrow \gamma_0(\text{carbon-deficient austenite}) + \kappa$ reaction occurred heterogeneously on the γ/γ grain boundaries. The κ phase is also an $(\text{Fe,Mn})_3\text{AlC}$ carbide, which was formed on the grain boundaries as a coarse particle. In contrast to the studies of the microstructures, the result concerning the mechanical properties of the austenitic FeAlMnC alloys with higher carbon content is very deficient. We are aware of only one article [15], in which the tensile properties of the Fe-15at.%Al-26at.%Mn-8at.%C (Fe-8.5wt.%Al-30wt.%Mn-2.0wt.%C) alloy was examined. However, their examinations were only focused on the alloy in the as-annealed condition or solution heat-treated and then aged at a high temperature of 800°C . Therefore, the main purpose of this study is an attempt to examine the tensile properties of the Fe-9wt.%Al-28wt.%Mn-1.8wt.%C alloy aged at 450°C .

2-2 Experimental Procedure

The Fe-9wt.%Al-28wt.%Mn-1.8wt.%C alloy was prepared in a vacuum induction furnace using pure Fe, Al, Mn and carbon powder. The melt was cast into a 20x30x100mm steel mold. After being homogenized at 1250°C for 24 h, the ingot was hot-rolled to a final thickness of 6 mm. The plate was subsequently solution heat-treated (SHT) at 1200°C for 2 h and then rapidly quenched into room-temperature water. Aging processes were carefully performed at 450°C for various times in a vacuum heat-treated furnace followed by rapid quenching. Transmission electron microscopy (TEM) and scanning electron microscopy (SEM) were used to investigate the microstructures and the tensile fracture surface as well as free surface. TEM specimens were prepared by using a double-jet electropolisher with an electrolyte of 60% acetic acid and 40% ethanol. Tensile tests were carried out at room-temperature with an Instron tensile testing machine at a strain rate of $6.7 \times 10^{-4} \text{ s}^{-1}$. Tensile test specimens were plates having 50 mm gauge length, 12 mm width and 5 mm thickness. The YS was measured at 0.2% offset strain.

2-3 Results and Discussion

In the as-quenched condition, the microstructure of the alloy was γ phase containing fine κ' carbides. The fine κ' carbides having an $L'1_2$ structure were formed within the γ matrix by spinodal decomposition during quenching. A typical microstructure is illustrated in Figure 2.1. This is similar to that observed by the present workers in the as-quenched Fe-9wt.%Al-30wt.%Mn-2.0wt.%C alloy [16]. When the as-quenched alloy was aged at 450°C for less than 9 h, the fine κ' carbides grew within the γ matrix and no grain boundary precipitates could be detected. An example is shown in Figure 2.2(a). Figure 2.2(b) is an SEM micrograph of the alloy aged at 450°C for 12 h, revealing that some small particles started to appear on the grain boundaries. Electron diffraction showed that the small particles were κ carbides. With increasing aging time at 450°C, the κ carbides grew into adjacent austenite grain through a $\gamma+\kappa' \rightarrow \gamma_0+\kappa$ reaction, as shown in Figure 2.2(c). In Figure 2.2(c), it is clearly seen that the mixture of ($\gamma_0+\kappa$) phases exhibited a lamellar structure.

Table 2.1 shows the tensile properties of the alloy in the as-quenched condition and aged at 450°C for various times. In Table 1, it is seen that the UTS, YS and elongation of the as-quenched alloy were 1080MPa, 868MPa and 55.5%, respectively. When the alloy was aged at 450°C for less than 9 h, the strength was pronouncedly increased and the elongation was slightly decreased with increasing the aging time. This is attributed to the growth of the κ' carbides within the γ matrix and no

precipitates on the grain boundaries. When the alloy was aged at 450°C for 12 h, the alloy could possess the high maximum UTS (1552MPa) and YS (1423MPa) with a good elongation of 25.8%. However, after prolonged aging at 450°C, both of the strength and ductility were drastically decreased. In order to characterize the relationship between the microstructures and tensile properties, the specimens after tensile test were examined by using SEM. Figure 2.3(a), a fractograph of the specimen aged at 450°C for 9 h, indicates ductile fracture with fine and deep dimples. Figure 2.3(b) is an SEM micrograph taken from the free surface in the vicinity of the fracture surface, showing that slip bands were generated over the specimen and some isolated tiny voids (indicated by arrows) were formed randomly within the grains. It is clear that these tiny voids strongly exhibited the self-stabilization under deformation. These observations are expected, because the specimen had a good elongation of 32.5%. In the specimen aged at 450°C for 12 h, the fractograph revealed that the dimples became coarser as well as shallower, and some dimples contain one or more coarse κ carbides (indicated by arrows), as illustrated in Figure 2.3(c). Figure 2.3(d), an SEM micrograph of the free surface, shows that small voids (indicated by arrows) appeared primarily along the grain boundaries. However, these small voids did not link up together. Therefore, under the highest strength condition, the specimen was still fairly ductile having a 25.8% elongation. However, the fracture surface and free surface of the specimen aged at 450°C for 15 h indicated that cracks occurred mainly along the grain boundaries due to the existence of the $(\gamma_o+\kappa)$ lamellar

structure, as shown in Figures 2.3(e) and (f). Apparently, the formation of the ($\gamma_0+\kappa$) lamellar structure on the grain boundaries deteriorated the ductility drastically.

Based on the preceding results, three important experimental results are discussed below. (I) Owing to contain a high density of fine κ' carbides within the austenite matrix, the yield strength (868MPa) of the present alloy in the as-quenched condition is much higher than that (410~551MPa) of the as-quenched FeAlMn(M)C ($C \leq 1.3\text{wt.}\%$) alloys [5-8]. Moreover, when the alloy was aged at 450°C for 9 h, the YS could reach up to 1383MPa with 32.5% elongation; aged for 12 h, the YS was 1423MPa and elongation was 25.8%. Compared to the previous studies, it is found that with almost equivalent ductility, the present alloy can possess yield strength about 28% higher than that of the FeAlMn(M)C ($C \leq 1.3\text{wt.}\%$) alloys after solution heat-treatment or controlled-rolling followed by the optimal aging at $450\sim 550^\circ\text{C}$ [8-13]. The result is probably that due to higher carbon content in the present alloy, a greater amount of fine κ' carbides could be formed within the austenite matrix during aging. (II) It is well-known that the austenitic FeAlMn(M)C alloys could possess a remarkable combination of strength and ductility due primarily to the formation of fine κ' carbides within the austenite matrix [8-13]. The as-quenched microstructure of the FeAlMn(M)C ($C \leq 1.3\text{wt.}\%$) alloys was γ phase or γ phase with small amount of (V, Nb)C carbides, and κ' carbides could only be formed during aging [1-13]. Therefore, the aging time required for attaining the optimal combination of strength and ductility was about 16 h at 550°C [8-13], and more than 500h at 450°C [10,12].

Whereas, the time of the present alloy aged at 450°C was only about 12 h, which was attributed to the pre-existing fine κ' carbides within the γ matrix in the as-quenched alloy. (III) In 2004, Kimura et al. reported that when the Fe-15at.%Al-26at.%Mn-8at.%C alloy was heat-treated at 1100°C and then furnace cooled to room temperature, the alloy showed almost zero ductility due to a lot of coarse κ carbides or/and thick κ carbide film on the grain boundaries [15]. To improve the ductility, they proposed a specific heat treatment: solution treatment at 1100°C for 1 h followed by water quenching, and subsequent aging at 800°C for 120 h. Through the specific heat-treatment, the microstructure was a mixture of ($\gamma_0 + \kappa$) lamellar structure. Consequently, the elongation could be improved to be about 12% with YS around 675MPa [15]. Evidently, the values of both strength and ductility are much lower than those obtained in the present alloy, and even lower than those obtained in the austenitic FeAlMn(M)C ($C \leq 1.3\text{wt.}\%$) alloys [8-13]. It is therefore suggested that the $\gamma + \kappa'$ structure is more favorable for both strength and ductility than the $\gamma_0 + \kappa$ lamellar structure.

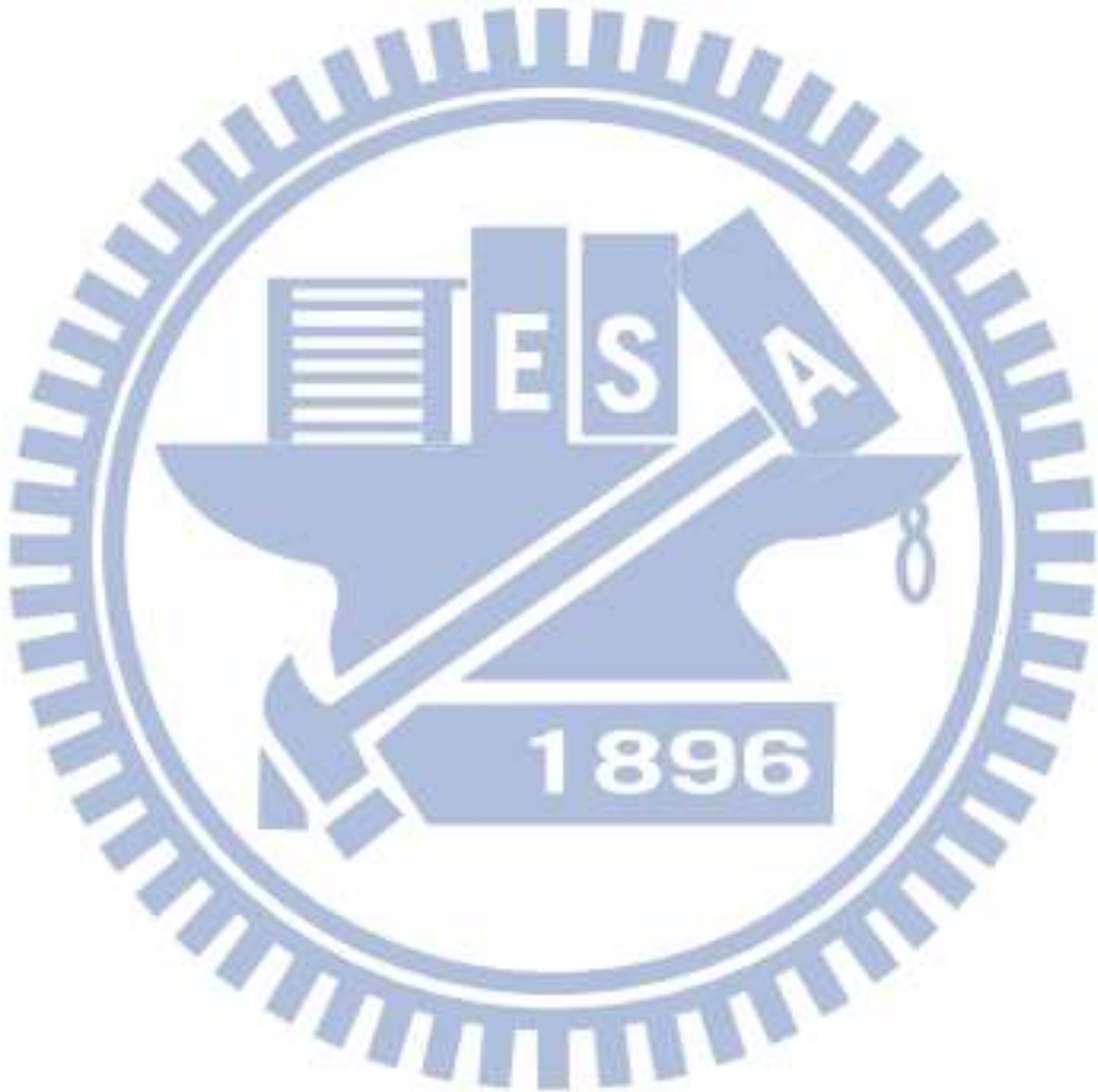
2-4 Conclusions

Optimal aging at 450°C, the Fe-9wt.%Al-28wt.%Mn-1.8wt.%C alloy could possess a high YS up to 1383MPa with a good 32.5% elongation. Under a similar ductility level, the YS was about 28% higher than that of the FeAlMn(M)C ($C \leq 1.3\text{wt.}\%$) alloys after solution heat-treatment or controlled-rolling followed by the optimal aging. In addition, due to the pre-existing of fine κ' carbides in the as-quenched alloy, the aging time required for attaining the optimal combination of strength and ductility was much less than that of the FeAlMn(M)C ($C \leq 1.3\text{wt.}\%$) alloys. When the present alloy was aged at 450°C for a time period longer than 12 h, both of the strength and ductility were drastically decreased due to the formation of the $(\gamma_0 + \kappa)$ lamellar structure on the grain boundaries.

References

- [1] S. M. Zhu, S. C. Tjong, *Metall. Mater. Trans. A* 29 (1998) 299.
- [2] C. N. Hwang, C. Y. Chao, T. F. Liu, *Scripta Metall.* 28 (1993) 263.
- [3] C. Y. Chao, C. N. Hwang, T. F. Liu, *Scripta Metall.* 28 (1993) 109.
- [4] S.C. Tjong, S.M. Zhu, *Mater. Trans.* 38 (1997) 112.
- [5] S.C. Chang, M. T. Jahn, *J. Mater. Sci.* 24 (1989) 1117.
- [6] H. J. Lai , C. M. Wan, *J. Mater. Sci.* 24 (1989) 2449.
- [7] E. K. James, *Metall. Trans. A* 19 (1988) 1873.
- [8] W. K. Choo, J. H. Kim, J. C. Yoon, *Acta Mater.* 45 (1997) 4877.
- [9] I. Kalashnikov, O. Ayselrad, A. Shalkevich, L. C. Pereira, *J. Mater. Eng. Perform.* 9 (2000) 597.
- [10] G. S. Krivonogov, M. F. Alekseyenko, G. G. Solov'yeva, *Fiz. Metall. Metalloved.* 39 (1975) 775.
- [11] I. S. Kalashnikov, B. S. Ermakov, O. Aksel'rad, L. K. Pereira, *Metall. Sci. Heat. Treat.* 43 (2001) 493.
- [12] I. S. Kalashnikov, O. Ayselrad, A. Shalkevich, L. D. Chumakova, L. C. Pereira, *J. Mater. Process. Tech.* 136 (2003) 72.
- [13] K. H. Han, *Mater. Sci. Eng. A* 279 (2000) 1.
- [14] Y. Kimura, K. Hayashi, K. Handa , Y. Mishima, *Mater. Sci. Eng. A* 329 (2002) 680.
- [15] Y. Kimura, K. Handa, K. Hayashi, Y. Mishima, *Intermetallics* 12 (2004) 607.

[16] C. S. Wang, C. N. Hwang, C. G. Chao, T. F. Liu, *Scripta Mater.* 57 (2007) 809.



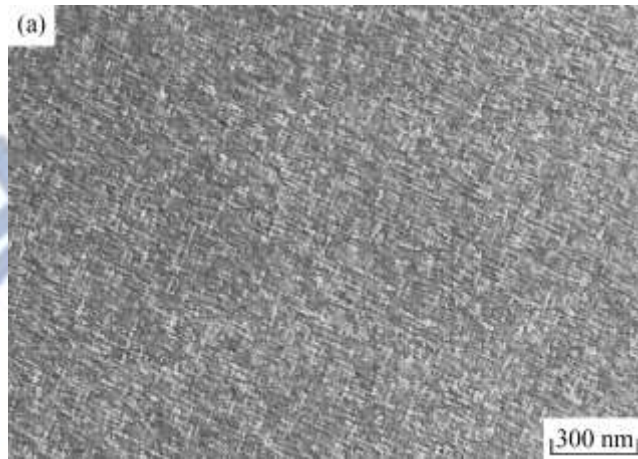


Figure 2.1(a)



Figure 2.1(b)

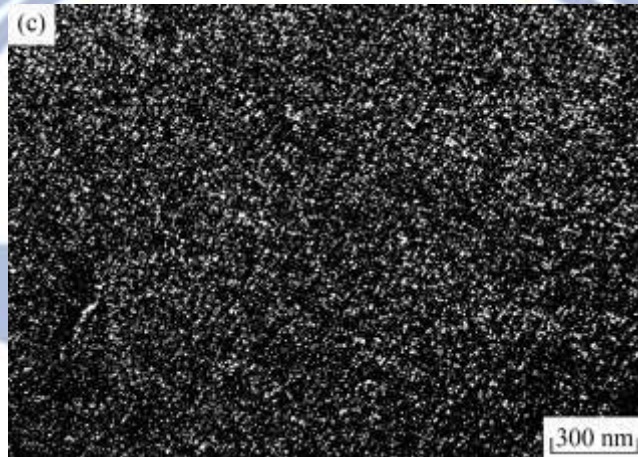


Figure 2.1(c)

Figure 2.1 Transmission electron micrographs of the as-quenched alloy: (a) bright-field image, (b) a selected-area diffraction pattern taken from the mixed region of austenite matrix and fine κ' carbides. The foil normal is $[001]_{\gamma}$ (hkl_{γ} : γ matrix; $hkl_{\kappa'}$: κ' carbide), and (c) $(100)_{\kappa'}$ dark-field image.

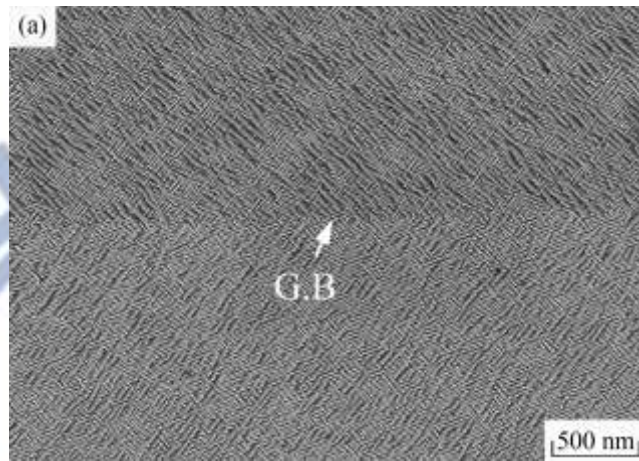


Figure 2.2(a)

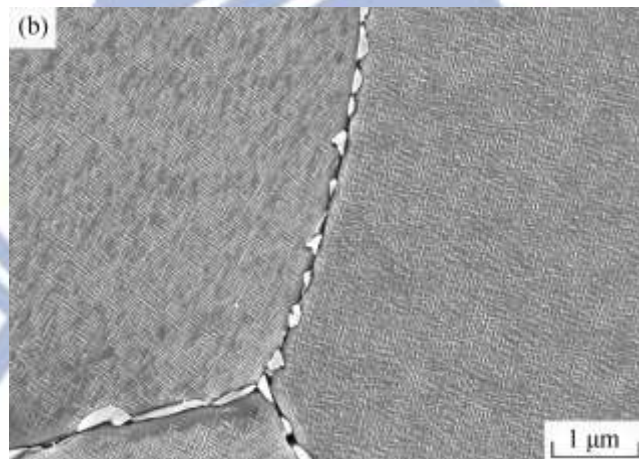


Figure 2.2(b)

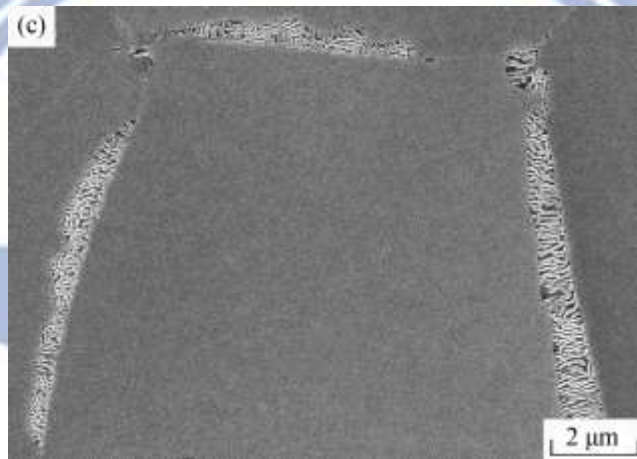


Figure 2.2(c)

Figure 2.2 Scanning electron micrographs of the alloy aged at 450°C for (a) 9 h, (b) 12 h, and (c) 15 h, respectively.

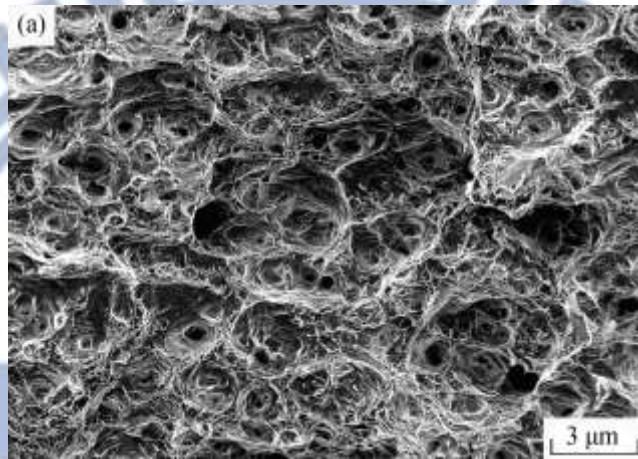


Figure 2.3(a)



Figure 2.3(b)

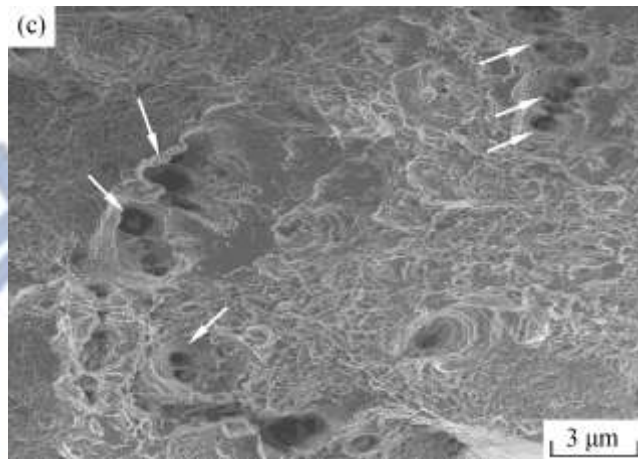


Figure 2.3(c)



Figure 2.3(d)

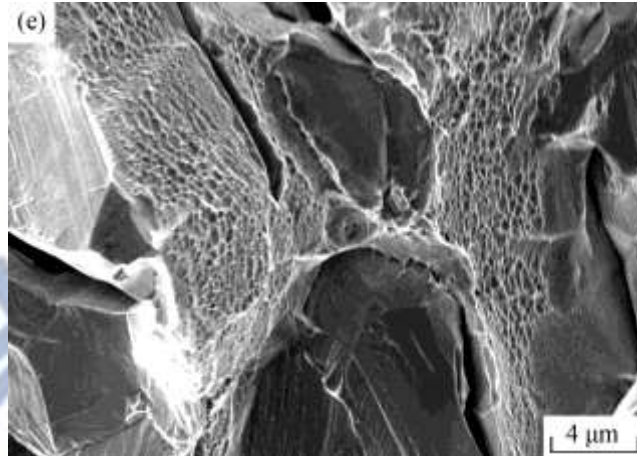


Figure 2.3(e)

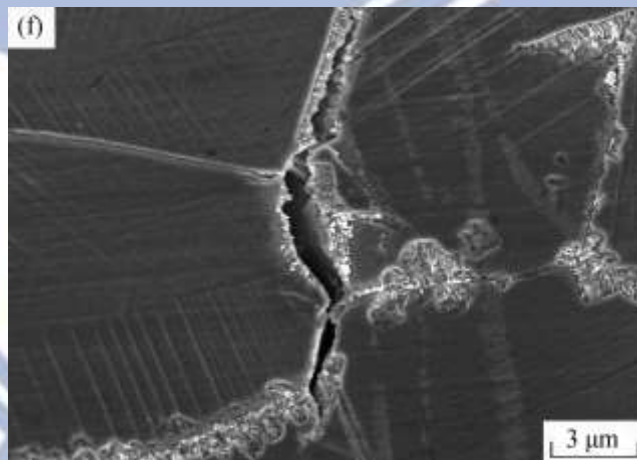
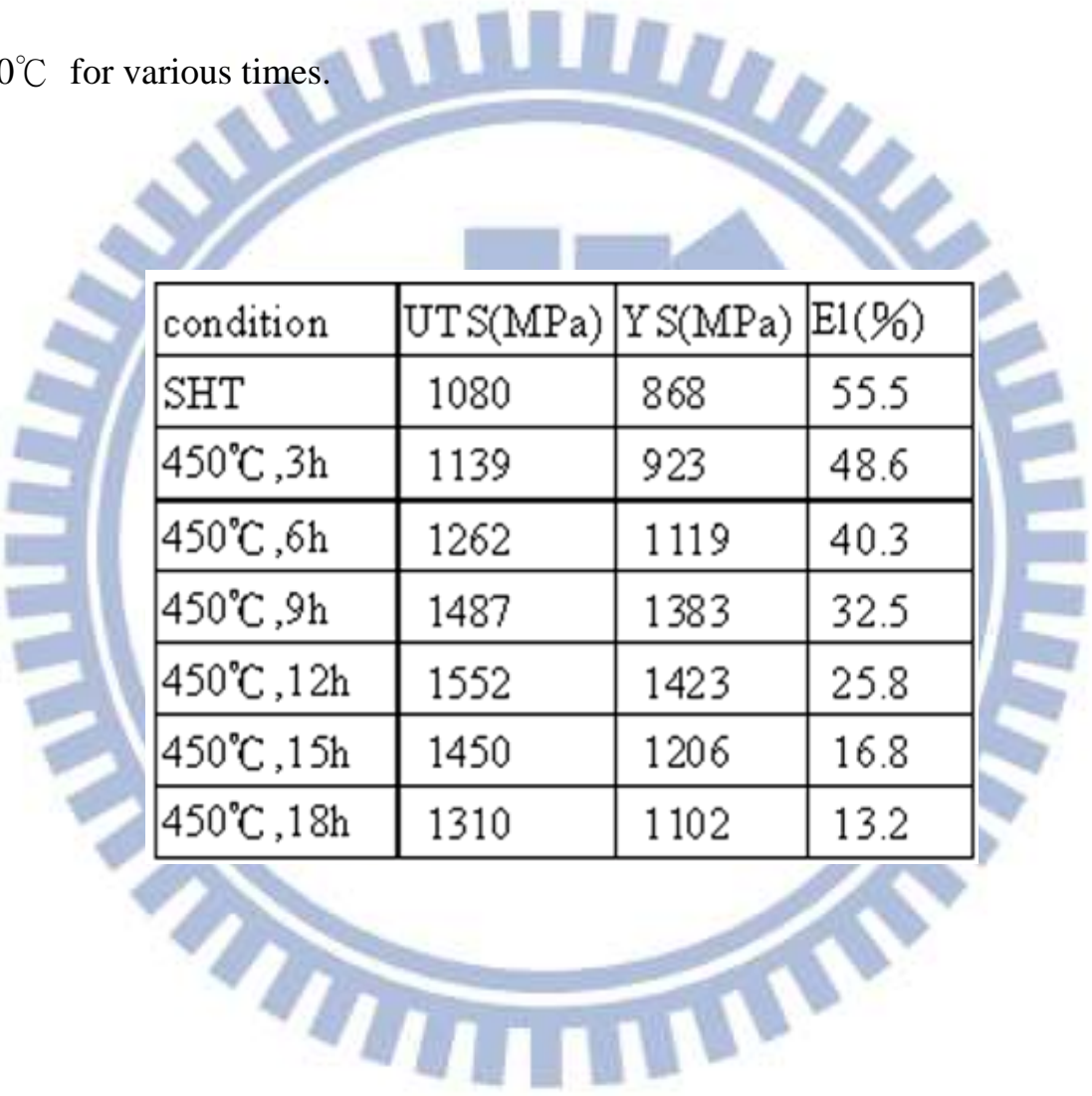


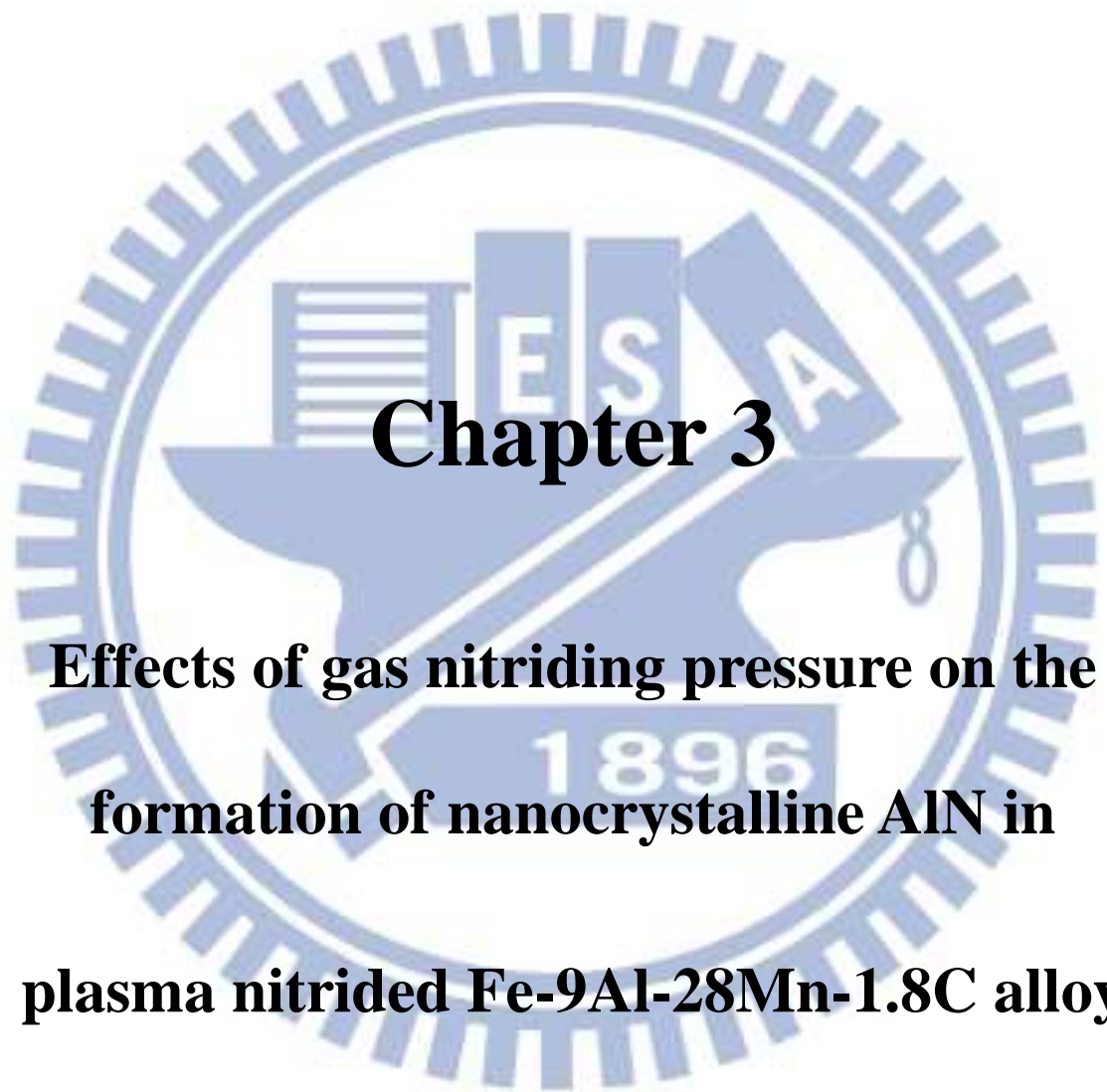
Figure 2.3(f)

Figure 2.3 Scanning electron micrographs taken from the tensile fracture surface and free surface, respectively, of the specimen aged at 450°C for (a)-(b) 9 h, (c)-(d) 12 h, and (e)-(f) 15h.

Table 2.1 Tensile properties of the alloy in the as-quenched condition and aged at 450°C for various times.



condition	UTS(MPa)	YS(MPa)	El(%)
SHT	1080	868	55.5
450°C ,3h	1139	923	48.6
450°C ,6h	1262	1119	40.3
450°C ,9h	1487	1383	32.5
450°C ,12h	1552	1423	25.8
450°C ,15h	1450	1206	16.8
450°C ,18h	1310	1102	13.2



Chapter 3

**Effects of gas nitriding pressure on the
formation of nanocrystalline AlN in
plasma nitrided Fe-9Al-28Mn-1.8C alloy**

Effects of gas nitriding pressure on the formation of nanocrystalline AlN in plasma nitrided Fe-9Al-28Mn-1.8C alloy

Abstract

The effects of gas nitriding pressure on the formation of nanocrystalline nitrided layer and its effect on the performance of the Fe-9Al-28Mn-1.8C alloy (in wt.%) were investigated. Plasma nitriding was conducted at 450 °C for 12h under nitriding pressures ranging from 133-798 Pa. The results evidently demonstrated that, due to the unique as-quenched microstructure of the present alloy, the effect of nitriding and aging could be achieved simultaneously with one-step plasma nitriding scheme. Both the thickness of nitrided layer and the nitrogen concentration at the outmost surface were found to increase with increasing the gas nitriding pressure in the range of 133-798 Pa. Detailed microstructural analyses indicated that the nitrided layer is composed predominantly of nanocrystalline face-centered-cubic (FCC) B1-AlN and FCC γ' -Fe₄N with minor amount of expanded austenite phase, which accounts for the excellent surface microhardness and corrosion resistance in 3.5% NaCl solution. The increase in gas nitriding pressure led to a thicker nitrided layer and smaller AlN particles, which in turn, resulted in higher surface microhardness and better corrosion resistance.

3-1 Introduction

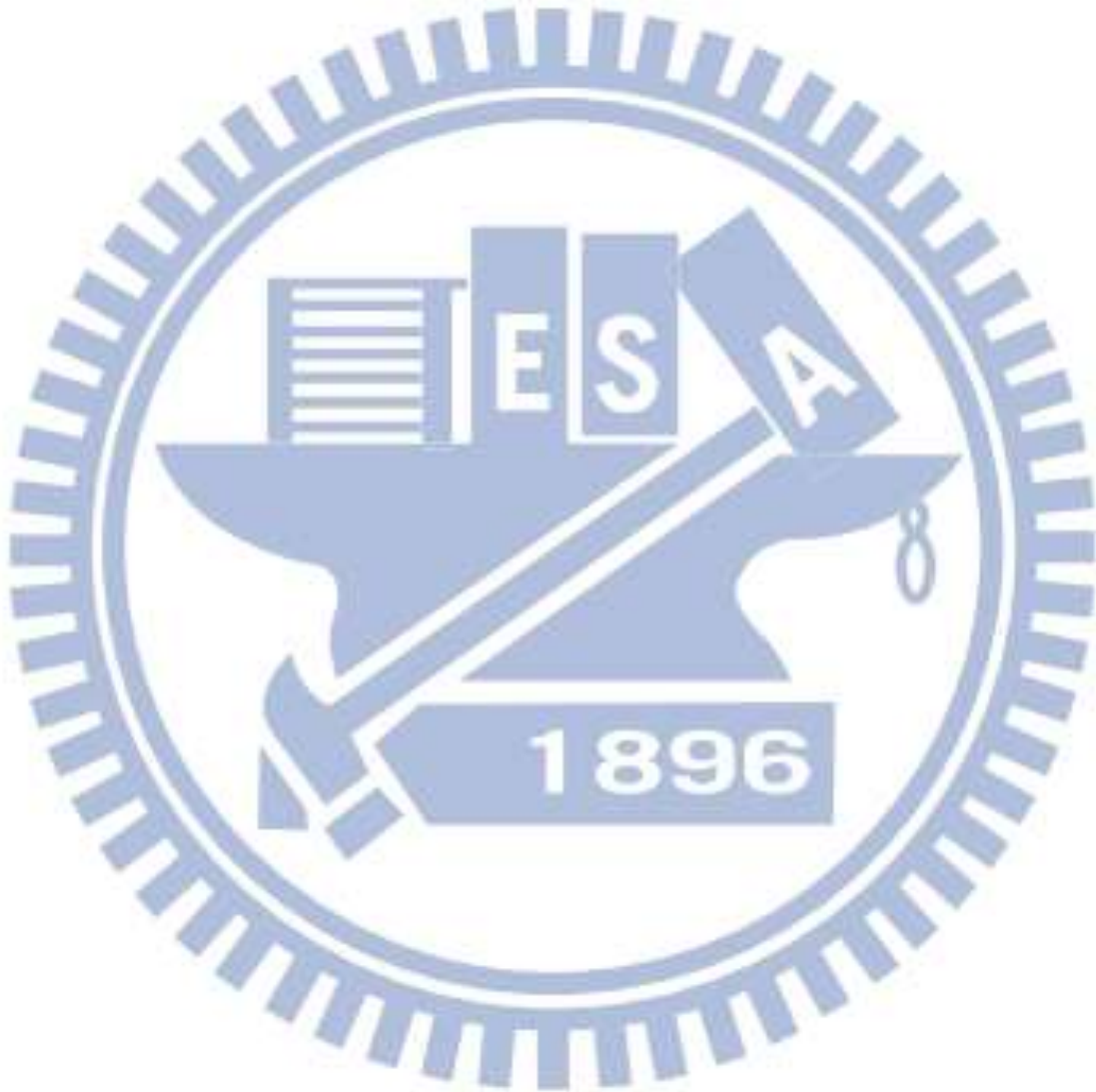
Plasma nitriding was widely used to improve the surface hardness and corrosion resistance of high-strength low-Cr (e.g. AISI 4140, 4340, and 5140) and high-Cr (e.g. AISI 410 martensitic and 17-4 PH precipitation-hardening stainless steels [1-7]). Prior to nitriding, these steels need to perform the following pre-heat treatment process: austenitizing, quenching and tempering at 15 °C above the nitriding temperature [8]. According to the extensive previous studies, the optimal nitriding conditions for the high-strength low-Cr steels were 520-550 °C for 4-6 h [1-3], while those for the high-strength high-Cr steels were 420-480 °C for 2-20 h [4-7]. The nitrated layer formed in these steels is mainly composed of expanded ferrite (α_N), Fe_3N (hexagonal close packed, HCP) and $\gamma'-Fe_4N$ (face-centered cubic, FCC), without or with a trace of CrN (FCC) [1-7]. After the optimal nitriding treatments, the surface microhardness of those nitrated steels could reach about 890~1204 Hv with $E_{corr} = -400 \sim -30$ mV and $E_{pit} = +50 \sim +800$ mV in 3.5% NaCl solution [1-7]. Obviously, plasma nitriding could considerably improve the surface microhardness and corrosion resistance of those high-strength steels. Unfortunately, such pre-heat treatment and high plasma nitriding temperature often deteriorated the substrate hardness to a low value of 210~400 Hv [1-7].

In contrast, the austenitic Fe-Al-Mn-C alloys could possess excellent combinations of strength and ductility. Previous studies have shown that the as-quenched microstructure of Fe-(7.8-9)Al-(28-30)Mn-(0.9-1.3)C ($C \leq 1.3$) alloys was single

austenite (γ) phase [9-12]. An optimal combination of strength and ductility could be obtained for the Fe-Al-Mn-C alloys aged at 550 °C for 15-16h [9-12], which was attributed to the precipitation of nano-sized (Fe, Mn)₃AlC carbides (κ' -carbides) having an L1₂ (ordered FCC) structure within the austenite matrix [9]. After optimal aging, the ultimate tensile strength (UTS), yield strength (YS) and elongation (El) could reach 1120-1230 Mpa, 900-1080 Mpa and 36-31%, respectively [9-12]. It is worthy to note that although the austenitic Fe-Al-Mn-C alloys could possess the remarkable combinations of strength and ductility, the corrosion resistance of these alloys in aqueous environments is not adequate for use in industrial applications [13-15]. However, comparing to the abovementioned commercially high-strength steels, information concerning the effects of nitriding on the Fe-Al-Mn-C alloy systems is very deficient [16]. Recently, we have shown that the as-quenched microstructure of the Fe-9Al-28Mn-1.8C (in wt.%) alloy was austenite phase containing an extremely high density of nano-sized (Fe,Mn)₃AlC carbides (κ' -carbides), which were formed by spinodal decomposition during quenching [17]. This is quite different from that observed in the austenitic Fe-Al-Mn-C ($C \leq 1.3$) alloys, in which nano-sized κ' -carbides could only be observed in the aged alloys [9-12]. The unique as-quenched microstructure has led to several attractive consequences. Firstly, due to the pre-existing nano-sized κ' -carbides, the aging temperature and time required to attain the optimal combination of strength and ductility were, respectively, much lower and less than those of the previous Fe-Al-Mn-C ($C \leq 1.3$) alloys, wherein the fine κ' -carbides could only be observed in the aged alloys thus prolonged aging at higher

temperatures were usually required, namely 550°C for 15~16h [9-12]. In contrast, with almost equivalent elongation, the Fe-9Al-28Mn-1.8C alloy can possess ~28% higher YS after being aged at 450 °C for merely 12h [17]. Secondly, it has been demonstrated that one could obtain tremendous improvements in surface microhardness, corrosion resistance, as well as excellent combination of strength and ductility simultaneously by simply performing one-step plasma nitriding treatment with the same temperature and time for optimal aging conditions. Specifically, the preliminary results obtained from a plasma nitrided Fe-8.68Al-30.5Mn-1.85C alloy at 500°C for 8h evidently exhibited excellent combinations of the surface hardness (1860 H_V), substrate hardness (550 Hv), ductility (33.6%) and pitting potential (E_{pit}) in 3.5% NaCl solution (+2030 mV) [16]. All of these properties are far superior to those obtained previously for the optimally gas-nitrided or plasma-nitrided high-strength alloy steels, as well as austenitic, martensitic and precipitation-hardening stainless steels [1-7, 18-21]. Nevertheless, according to our previous study [17], it was found that after being aged at 450 °C for 12h, the Fe-9Al-28Mn-1.8C alloy could achieve the best combination of UTS, YS and El. Thus, it is worthwhile to explore how the surface hardness, corrosion resistance and mechanical properties of the alloy can be simultaneously optimized by one-step plasma nitriding scheme. Furthermore, it is well established that the gas nitriding pressure plays an essential role in plasma nitriding treatments of various steels [22-24]. In the present study, in order to achieve the effects of aging and nitriding simultaneously, the plasma nitriding treatments of the Fe-9Al-28Mn-1.8C alloy were fixed at 450°C for 12h and the same gas

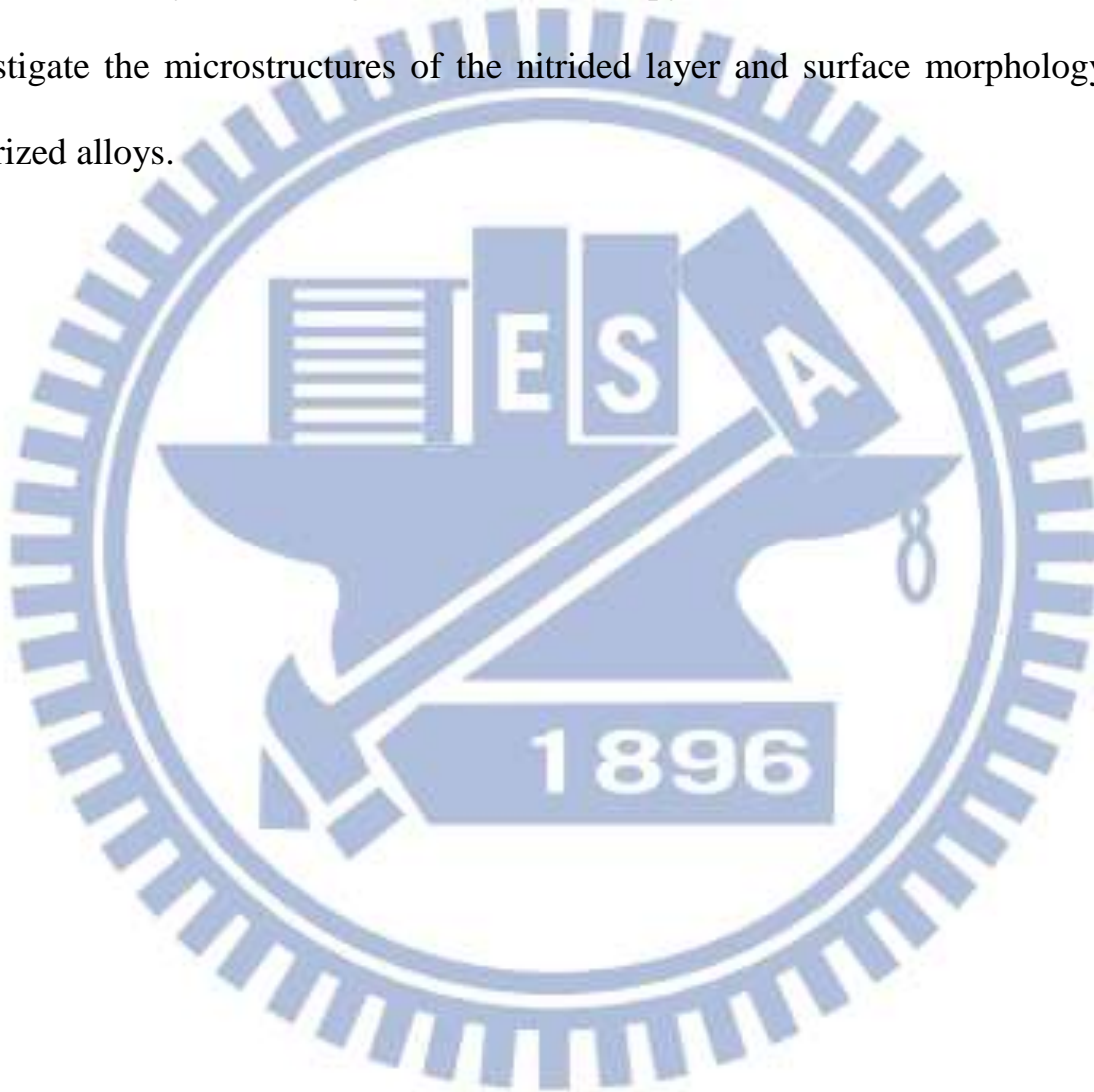
composition with various nitriding pressures were used. It is worth noting that, to date, little information concerning the effects of nitriding pressure on the structures and properties of the plasma nitrided Fe-Al-Mn-C alloys has been reported in the literature.



3-2 Experimental Procedure

The Fe-9Al-28Mn-1.8C alloy was prepared in an air induction furnace by using pure Fe, Al, Mn and carbon powder. The melt was cast into a 30 mm×50 mm×150 mm steel mold. After being homogenized at 1200 °C for 6h, the ingot was hot-rolled to a 6.5 mm thick plate. The plate was subsequently solution heat-treated at 1150 °C for 2h and then quenched into room-temperature water. Prior to nitriding treatments, the plate was cut into pieces of size 10 mm×10 mm×5 mm. These pieces were polished using SiC papers to 2400 grit and then with 1.5 μm Al₂O₃ powder, washed in distilled water. The plasma nitriding treatments were carried out using a 20-kW pulsed DC plasma nitriding equipment. Prior to nitriding process, the treatment chamber was pumped down to a base pressure of ~10⁻⁴ Pa. The plasma nitriding processes were performed at 450 °C for 12h using an atmosphere of 50% N₂ and 50% H₂ under a gas pressure of 133, 399 and 798 Pa, respectively. X-ray diffraction (XRD) was carried out to identify the phase of the nitrided layer using a Bruker D8 with Cu-Kα radiation with an incident grazing angle of ~2-3°. The depth-dependent nitrogen concentration and microhardness of the nitrided alloy were determined by using glow discharge spectrometer (GDS, LECO-GDS-750A) and Vicker's indenter (Matsuzawa, Digital Microhardness Tester Mode MXT-α 7e) at 100 gf, respectively. The microhardness tests were carried along the cross section of the nitrided alloys with every individual indentation being about 1 μm apart to avoid the mutual interferences. Potentiodynamic polarization curves were measured in 3.5% NaCl solution at 25 °C

with a scan rate of 2 mV s^{-1} . A saturated calomel electrode (SCE) and a platinum wire were used as reference and auxiliary electrodes, respectively. At least 3 repeated corrosion experiments were performed on each condition. A 5% nital solution was used as the etching protocol to reveal the microstructure and surface morphology of the nitrided alloys. Scanning electron microscopy (SEM, JOEL-6500F) was used to investigate the microstructures of the nitrided layer and surface morphology of the polarized alloys.



3-3 Results and Discussion

Figure 3.1 (a)-(c) are the cross-sectional SEM images of the alloy after plasma nitriding at 450 °C for 12h under the nitriding gas pressure of 133, 399 and 798 Pa, respectively. The thickness of the nitrided layer is approximately 6, 9 and 15 μm for gas pressure of 133, 399 and 798 Pa, respectively. The results indicate that within the present pressure range, the nitriding efficiency increases with increasing gas pressure. It is also evident that near the surface of the nitrided layer there exists a bright thin layer whose thickness is about 0.5, 1.0 and 1.4 μm for nitriding pressure of 133, 399 and 798 Pa, respectively. As will be shown below, this thin bright layer may be attributed to a layer of nano-crystalline FCC B1-AlN. Moreover, it is noted that the γ grain boundary of the substrate are clearly revealed by the 5% nital etchant, while nitrided layer appears to be very homogeneous morphologically and the interface between the nitrided layer and the γ matrix is very obscure. This is markedly different from that observed in nitrided high-strength alloy steels and austenitic, martensitic stainless steels as well as precipitation-hardening stainless steels, wherein “dark lines” resulted from nital etching could be observed at the interface between nitrided layer and substrate [3-7]. This may be attributed to the very different crystal structure between the constituent phases in the nitrided layer and that of the matrix. In the present nitrided alloys, the primary constituent phases in the nitrided layer (FCC B1-AlN and FCC γ' -Fe₄N) and substrate (γ matrix and κ' -carbides) are all of FCC-type structure [25-29] with very similar lattice parameters. This is in sharp contrast to

high-strength alloy and various stainless steels, wherein the primary constituent phases in nitrated layer are Fe_3N (HCP), γ' - Fe_4N (FCC), and/or CrN (FCC), which do not have a good lattice matching with the matrix. As a result, the interfaces are usually incoherent and accompanied with tremendous strain, resulting in clear “dark lines” between the nitrated layer and matrix after etching [3-7].

Figure 3.2 shows the XRD results of the nitrated alloys treated with the gas pressure of 133, 399 and 798 Pa, respectively. For comparison, the XRD profile obtained from the solution heat-treated (without nitrating) alloy is also displayed in Figure 3.2. There are several distinct features immediately noticed in these XRD results. **(i)** The results clearly show that the nitrated layer is composed predominantly of FCC AlN and relatively smaller amount of FCC γ' - Fe_4N [25-29]; both phases have the same FCC-type structure as the γ matrix. **(ii)** The intensity of the γ -phase diffraction peaks is decreased with increasing gas nitrating pressure, which is consistent with the trend of gas nitrating pressure dependence of nitrated layer thickness. **(iii)** In addition to the apparent broadening, the γ -phase diffraction peaks in the nitrated alloys also exhibit noticeable shift to lower diffraction angles, indicating the existence of expanded γ -phase (γ_{N}) in the nitrated layer, which is similar to that reported by other authors in the plasma-nitrated austenitic stainless steels [19-20]. It is noted that the diffraction peak corresponding to (111) plane of γ' - Fe_4N near $2\theta \sim 40^\circ$ appears to be slightly asymmetric, which might be attributed to the influence from γ_{N} phase. The lattice parameters for the γ , γ_{N} , AlN , and γ' - Fe_4N as obtained from the XRD

patterns for the untreated and nitrided alloys under pressure of 133, 399 and 798 Pa are $a_{\gamma} \sim a_{\gamma_N} = 0.367 \sim 0.372$ nm, $a_{\text{AlN}} = 0.403 \sim 0.404$ nm and $a_{\gamma\text{-Fe}_4\text{N}} = 0.381 \sim 0.383$ nm, respectively. (iv) In contrast to those seen in γ_N , although the diffraction peaks of AlN and $\gamma\text{-Fe}_4\text{N}$ also display tremendous broadening, the corresponding diffraction angles of these peaks do not show noticeable shift. The possible reason for this difference is that the off-stoichiometry tolerance of nitrogen concentration in both AlN and $\gamma\text{-Fe}_4\text{N}$ is very limited [30]. Thus, no discernible diffraction angle shift and solute-induced peak broadening would be expected. Consequently, the peak broadening must have originated from factors other than that occurring in γ_N . One of the most common origins of XRD peak broadening is the reduced particle size, especially when it is smaller than sub-micron size. Under this circumstance, the particle size can be calculated from the full-width at half-maximum (FWHM) of the primary diffraction peak by using the Scherrer's formula [31]: $D = K\lambda/\beta\cos\theta$, where D is the particle size, K (~ 0.9) is a constant, λ is the wavelength, β and θ is the FWHM and angle of the chosen diffraction peak, respectively. Taking the (111) diffraction peak of AlN as an example, the particle size for AlN in the nitrided layer is approximately 14.0 ± 0.6 nm, 9.0 ± 0.4 nm, and 8.0 ± 0.4 nm for gas nitriding pressure of 133, 399 and 798 Pa, respectively, which is very good agreement with the SEM observations (see below). Similarly, the particle size of $\gamma\text{-Fe}_4\text{N}$ has been determined to be 19.0 ± 0.8 nm, 14.0 ± 0.6 nm, and 12.0 ± 0.4 nm, for gas nitriding pressure of 133, 399 and 798 Pa, respectively. The effect of gas nitriding pressure on the particle size is believed to

arise from the strong nitrogen affinity of Al, which may have effectively facilitated the nucleation of AlN at higher gas pressures during nitriding. For instance, Jeong and Kim [32] used optical emission spectroscopy to quantitatively determine the ratio between the active N_2^+ species and N_2 as a function of nitriding pressure in glow discharge plasma nitriding of M2 high speed steels and found that the N_2^+/N_2 ratio increased from 11.33 to 19.0 when the nitriding pressure was increased from 133 to 798 Pa. As a consequence, the thickness of the nitrided layer in their study increased significantly with increasing nitriding pressure [32]. This is also consistent with the recent theoretical study performed by Van Landeghem et al. [33], wherein high driving force for nitride nucleation induced by the high level of nitrogen in solid solution was evidently demonstrated. Our results are apparently in good agreement with their observations and predictions.

In order to delineate how the gas nitriding pressure affects the diffusion of nitrogen and associated phases formed in the nitrided layer, nitrogen concentration depth profiles were measured by GDS analysis and the results are shown in Figure 3.3 (a). It is apparent from Figure 3.3 (a) that the surface concentration of nitrogen increases with increasing gas pressure reaching ~18.4 wt.% (~44.3 at.%) at the surface for the 798 Pa case. The diffusion depth also matches with the thickness of nitrided layer seen in Figure 3.1 (a)-3.1 (b). It is seen in Figure 3.3 (a) that the surface nitrogen concentration does not reach stoichiometric 50 at.% for pure AlN, suggesting that γ' - Fe_4N and perhaps a small amount of γ_N phase are simultaneously formed on the top

surface layer. In this scenario, the similar depth dependence displayed in the nitrogen concentration (Figure 3.3 (a)) and the corresponding microhardness (Figure 3.3 (b)) depth profiles may be attributed to the varying amount of the three constituent phases identified in the nitrided layer. Since the hardness of the pristine AlN and γ' -Fe₄N phase is 23.6-25.7 GPa [34, 35] and 8.6-11.2 GPa [36, 37], respectively, the slightly decreasing trend of microhardness might imply that the relative amount of AlN decreases continuously with the increasing depth. Alternatively, it has been indicated that, in most nitriding treatments, the nitrided layer is usually composed of a compound layer and a diffusion layer [29]. It is likely that the nitrogen concentration gradient may also lead to variations in both the relative amount of constituent phases and the exact composition of the constituent phase itself.

Figure 3.4 (a)-3.4 (c) show the SEM surface images of the alloy nitrided under the nitriding gas pressure of 133, 399 and 798 Pa, respectively. It is evident from these images that the nitrided layer appears to compose of two different nano-sized particles, whose size becomes smaller with increasing nitriding pressure. Since γ' -Fe₄N is believed to be more prone to nital etching than AlN, we assume that particles with lighter appearance are AlN and the darker ones are γ' -Fe₄N. Based on this assumption, the average particle size and volume fraction of the AlN nitride obtained using a LECO2000 image analyzer were determined to be 14.3±0.7 nm, 71.5±0.6%; 9.6±0.5 nm, 77.1±0.5% and 8.3±0.5 nm, 80.3±0.8% for the alloy treated under the nitriding pressure of 133, 399 and 798 Pa, respectively. It is clearly seen that the

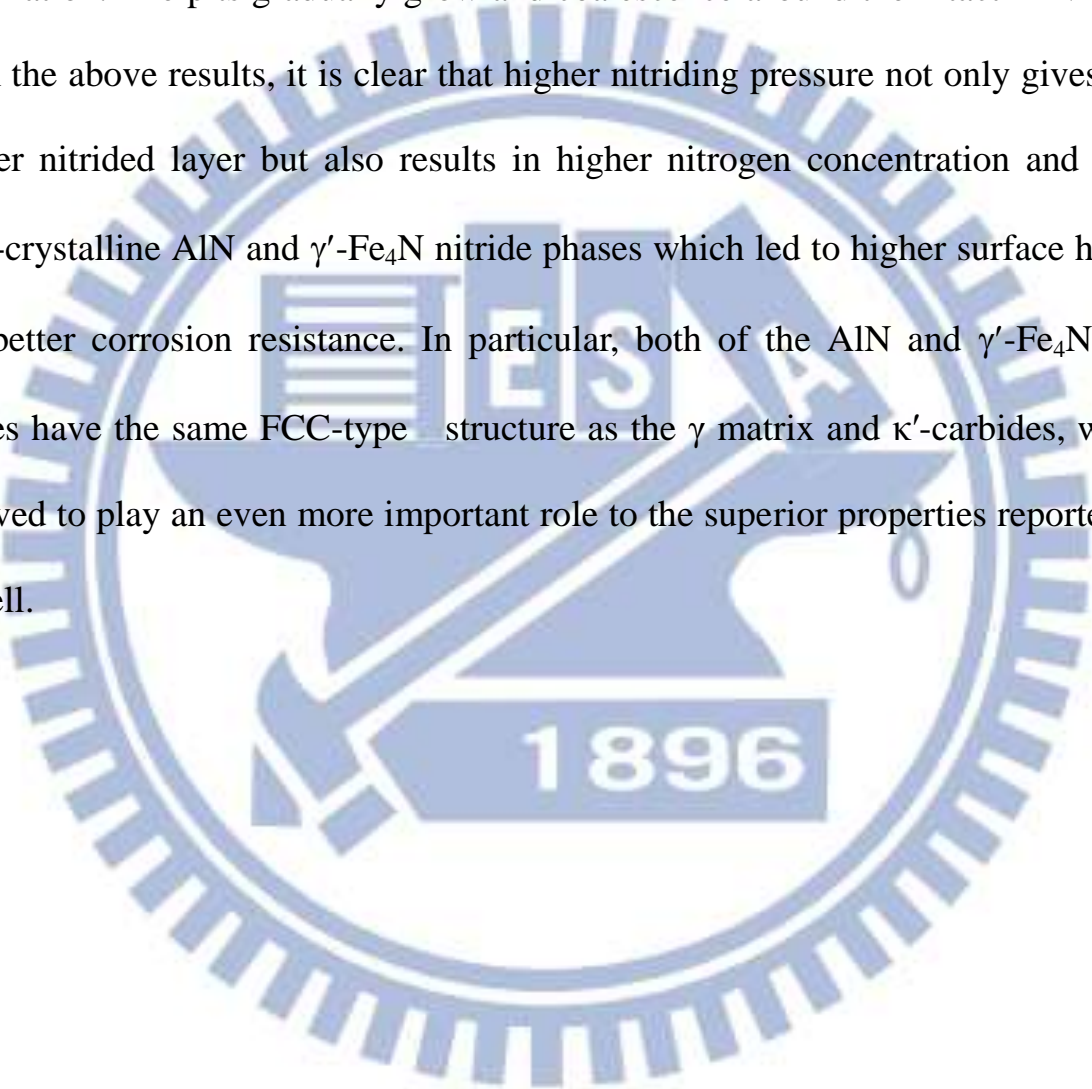
average particle sizes of the AlN nitride determined from the image analyses are very approximate to those obtained from XRD results (Figure 3.2), namely 14.0 ± 0.6 nm, 9.0 ± 0.4 nm, and 8.0 ± 0.4 nm, respectively. It is therefore proposed that under the current nitriding pressure range, the volume fraction increased and the average particle size pronouncedly decrease of the AlN nitride, which has led to possess the highest microhardness for the 798 Pa case. The surface hardness obtained in all of the present nitrided alloys is slightly lower than the value of ~ 1800 Hv reported in ion nitrided LDX2101 duplex stainless steel [38] and nitrogen-carbon glow discharged AISI 304 and AISI 316L steels [39]. Nevertheless, it is substantially higher than obtained in optimally nitrided alloy steels and various stainless steels, wherein the surface hardness ranging from 890 to 1350 Hv was obtained [1-7,18-21]. Moreover, the estimated volume fraction of AlN, which are summarized together with the particle size in Table 3.1, also indicates an apparent increasing tendency with increasing nitriding pressure. These again are consistent with our conjecture of attributing the obtained surface microhardness variations to nitrogen concentration and the relative amount of constituent phases existing in the nitrided layer resulted from different nitriding pressures. Finally, we note that the hardness of the matrix remains as high as 600 Hv regardless the values of nitriding gas pressure used, indicating that the aging effect is indeed depending only on the temperature and time and is not influenced by the nitriding pressure. It is noted that the hardness of the matrix in the present case is also higher than that (~ 550 Hv) obtained from the same alloy nitrided at 500°C for 8h reported previously [16].

Next we turn to discuss the corrosion resistance performance of the nitrided layer obtained with different nitriding pressures. Potentiodynamic polarization curves in 3.5% NaCl solution for the un-treated alloy and the alloys nitrided under different nitriding pressures are shown in Figure 3.5 (a). The electrochemical parameters including corrosion current density (I_{corr}), pitting corrosion current density (I_p), corrosion potential (E_{corr}) and pitting potential (E_{pit}) for the un-treated and the nitrided alloys are summarized in Table 3.1, It is evident from the results shown in Figure 3.5 (a) and Table 3.1 that, for the un-treated alloy, there is no apparent passivation region with I_{corr} and E_{corr} being 8.2×10^{-6} A/cm² and -782 mV, respectively. This is indicative that the predominant mechanism prevailing in the untreated alloy is general corrosion. Consequently, no pitting potential could be identified in this case [40]. On the other hand, nitriding at 450 °C for 12h apparently has significantly improved the corrosion resistance of the alloy. Specifically, not only an obvious passivation region appears in the polarization curve, but also I_{corr} has been reduced by more than three orders of magnitude from 8.2×10^{-6} A/cm² (untreated alloy) to 2.4×10^{-9} A/cm² (798 Pa). Moreover, E_{corr} is also improved from -782 mV to +30 ~ +58 mV with E_{pit} ranging from +1360 mV to +1765 mV for the nitrided alloys. The overall surface microhardness and corrosion resistance of the present study are slightly lower than those nitrided at higher temperature as reported previously (surface hardness \approx 1860 Hv and $E_{\text{pit}} \approx$ +2030 mV) [16], because of the differences in thickness and relative amount of constituent phases in the nitrided layer. Nevertheless, far superior than those obtained previously in optimally nitrided high-strength alloy steels, as well

as austenitic, martensitic and precipitation-hardening stainless steels [1-7, 18-21], wherein $E_{\text{corr}} \approx -450 \sim -30$ mV and $E_{\text{pit}} \approx -150 \sim +1200$ mV had been obtained under similar polarization tests in 3.5% NaCl solution.

To further delineate how the corrosion pits develops during the polarization test, the surface morphologies of the polarized untreated alloy and plasma nitrided alloys are displayed in Figure 3.5 (b)-(d), respectively. The SEM images clearly reveal that, without the protection of the nano-crystalline nitrided layer, the grain boundaries and austenite matrix of the untreated alloy were severely attacked during polarization, indicating again that general corrosion has been the dominant mechanism in this case [40]. On the other hand, only very small corrosion pits with dimensions of about 15~20 nm-wide and 50~200 nm-long were formed for the alloys being nitrided with nitriding pressure of 133 and 798 Pa (as indicated by arrows shown in Figure 3.5 (c)-(d).) It is worthy noting that the size of the pits is much smaller than that (30~300 μm) observed in the optimally nitrided alloy steels and various stainless steels under similar polarization tests [2-3, 5-7]. The detailed corrosion mechanism operating in these nitrided alloys is not clear at present. Nevertheless, comparing to the surface morphology prior to polarization test displayed in Figure 3.4, the corrosion pits appear to develop preferentially on certain phase during polarization. Although there is no direct evidence indicating which phase is more prone to corrosion in 3.5% NaCl solution, we believe that it is γ' -Fe₄N which being attacked preferentially to form the corrosion pits. In the previous studies [4, 41-42], it was reported that both the surface

hardness and the corrosion resistance of nitrides are very much dependent on the nitrogen concentration containing in the compound. It is therefore plausible to expect that AlN is much harder and more resistive to corrosion than γ' -Fe₄N, suggesting that the corrosion pits develop preferentially from the γ' -Fe₄N particles during polarization. The pits gradually grow and coalesce around the intact AlN regions. From the above results, it is clear that higher nitriding pressure not only gives rise to thicker nitrated layer but also results in higher nitrogen concentration and smaller nano-crystalline AlN and γ' -Fe₄N nitride phases which led to higher surface hardness and better corrosion resistance. In particular, both of the AlN and γ' -Fe₄N nitride phases have the same FCC-type structure as the γ matrix and κ' -carbides, which is believed to play an even more important role to the superior properties reported here, as well.



3-4 Conclusions

In summary, effects of nitriding gas pressure on the structure and properties of plasma nitrided Fe-9.8Al-29Mn-1.8C alloy were systematically investigated. The results indicated that, within the pressure range (133~798 Pa) investigated in this study, both the thickness of the nitrided layer and the surface concentration of nitrogen are increased with increasing nitriding pressure. The fact that, both of the nitrogen concentration and hardness depth profiles are all behaving similarly in the pressure range studied, indicating that the nitrogen in-diffusion and the associated phase formation mechanisms within the nitrided layer are the same. The excellent surface hardness and corrosion resistance exhibited by the nitrided alloys are attributed to the formation of nitrided layer composed predominantly of nano-crystalline FCC B1-AlN and FCC γ' -Fe₄N with minor amount of expanded austenite phase, resulting in coherent interfaces between the nitrided layer and γ matrix. The increased nitriding pressure might have facilitated the nucleation of nitrides, which, in turn, leads to a smaller particle size of the nano-crystalline phases in nitrided layer.

References

- [1] Y. Li, L. Wang, D. Zhang, L. Shen, J. Alloys. Compd. 497 (2010) 285.
- [2] T. Savisalo, D. B. Lewis, Q. Luo, M. Bolton, P. Hovsepian, Surf. Coat. Technol. 202 (2008) 1661.
- [3] Y. Li, L. Wang, D. Zhang, L. Shen, Appl. Surf. Sci., 256 (2010) 4149.
- [4] P. Corengia, G. Ybarra, C. Moina, A. Cabo, E. Broitman, Surf. Coat. Technol. 187 (2004) 63.
- [5] C. X. Li, T. Bell, Corrosion Science 48 (2006) 2036.
- [6] R. L. Liu, M. F. Yan, Mater. Des. 31 (2010) 2355.
- [7] R. L. Liu, M. F. Yan, Surf. Coat. Technol. 204 (2010) 2251.
- [8] Cubberly, W.H., Masseria, V., Kirkpatrick, C.W. and Sanders B. Metals Handbook, ninth ed., Heat Treating, vol. 4, American Society for Metals, Metals Park, OH, 1982.
- [9] W. K. Choo, J. H. Kim, J. C. Yoon, Acta Mater. 45 (1997) 4877.
- [10] I. Kalashnikov, O. Ayselrad, A. Shalkevich, L. C. Pereira, J. Mater. Eng. Perform. 9 (2000) 597.
- [11] G. S. Krivonogov, M. F. Alekseyenko, G. G. Solov'yeva: Fitz. Metal. Metalloved 39 (1975) 775.

[12] I. S. Kalashnikov, O. Acselrad, A. Shalkevich, L. D. Chumakova and L. C. Pereira: J. Mater. Process Tech. 136 (2003) 72.

[13] S.C. Chang, J.Y. Liu, H.K. Juang, Corrosion. Eng. 51 (1995) 399.

[14] C.J.Wang, Y.C. Chang, Mater. Chem. Phys. 76 (2002) 151.

[15] X.M. Zhu, Y.S. Zhang, Corrosion 54 (1998) 3.

[16] P. C. Chen, C. G. Chao, T. F. Liu, Scripta Mater. 68 (2013) 380.

[17] K. M. Chang, C. G. Chao, T. F. Liu, Scripta Mater. 63 (2010) 162.

[18] C. X. Li, T. Bell, Corrosion Science 46 (2004) 1527.

[19] H. R. Abedi, M. Salehi, Mater Des 32 (2011) 2100.

[20] M. Olzon-Dionysio, S. D. de Souza, R. L. O. Basso, S. de Souza, Surf. Coat. Technol. 202 (2008) 3607.

[21] L. Shen, L. Wang, Y. Wang, C. Wang, Surf. Coat. Technol. 204 (2010) 3222.

[22] A. Nishimoto, K. Nagatsuka, R. Narita, H. Nii, K. Akamatsu, J. ASTM International 8 (2011) Paper ID: JAI103286.

[23] F. Borgioli, A. Fossati, E. Galvanetto, T. Bacci, G. Pradelli, Surf. Coat. Technol. 200 (2006) 5505.

[24] S. D. de Souza, M. Kapp, M. Olzon-Dionysio, M. Campos, Surf. Coat. Technol.

204 (2010) 2976.

[25] M. Wen, H. Huang, K. Zhang, Q. Meng, X. Li, L. Kong, Surf. Coat. Technol.

235 (2013) 367.

[26] R.F. Zhang, S. Veprek, Acta Mater. 55 (2007) 4615.

[27] S.H. Sheng, R.F. Zhang, S. Veprek, Acta Mater. 45 (1997) 4877.

[28] M. Moradshahi, T. Tavakoli, S. Amiri, Sh. Shayeganmehr, Surf. Coat. Technol.

201 (2013) 567.

[29] Z. Q. Liu, Z. K. Hei, D. X. Li, J. Mater. Res. 17 (2002) 2621.

[30] H. A. Wriedt, N. A. Gokcen, R. H. Nafziger, Bull. Alloy Phase Diagram 8 (1987).

355.

[31] B. D. Cullity and S. R. Stock, *Element of X-ray Diffraction*, Prentice-Hall, New

Jersey, 2011, p. 170.

[32] B.Y. Jeong and M. H. Kim, Surf. Coat. Technol. 141 (2001) 182.

[33] H. P. Van Landeghem, M. Gouné, and A. Redjaïmia, J. Crystal Growth 341

(2012) 53.

[34] G. S. Kim, S. Y. Lee, J. H. Hahn, S. Y. Lee, Surf. Coat. Technol. 171 (2003) 91.

[35] J. K. Park, Y. J. Baik, Mater. Lett. 62 (2008) 2528.

[36] H. A. Wriedt, N. A. Gokcen, R. H. Nafziger, Bull. Alloy Phase Diagram 8 (1987).

355.

[37] E. A. Ochoa, C. A. Figueroa, F. Alvarez, Surf. Coat. Technol. 200 (2005) 2165.

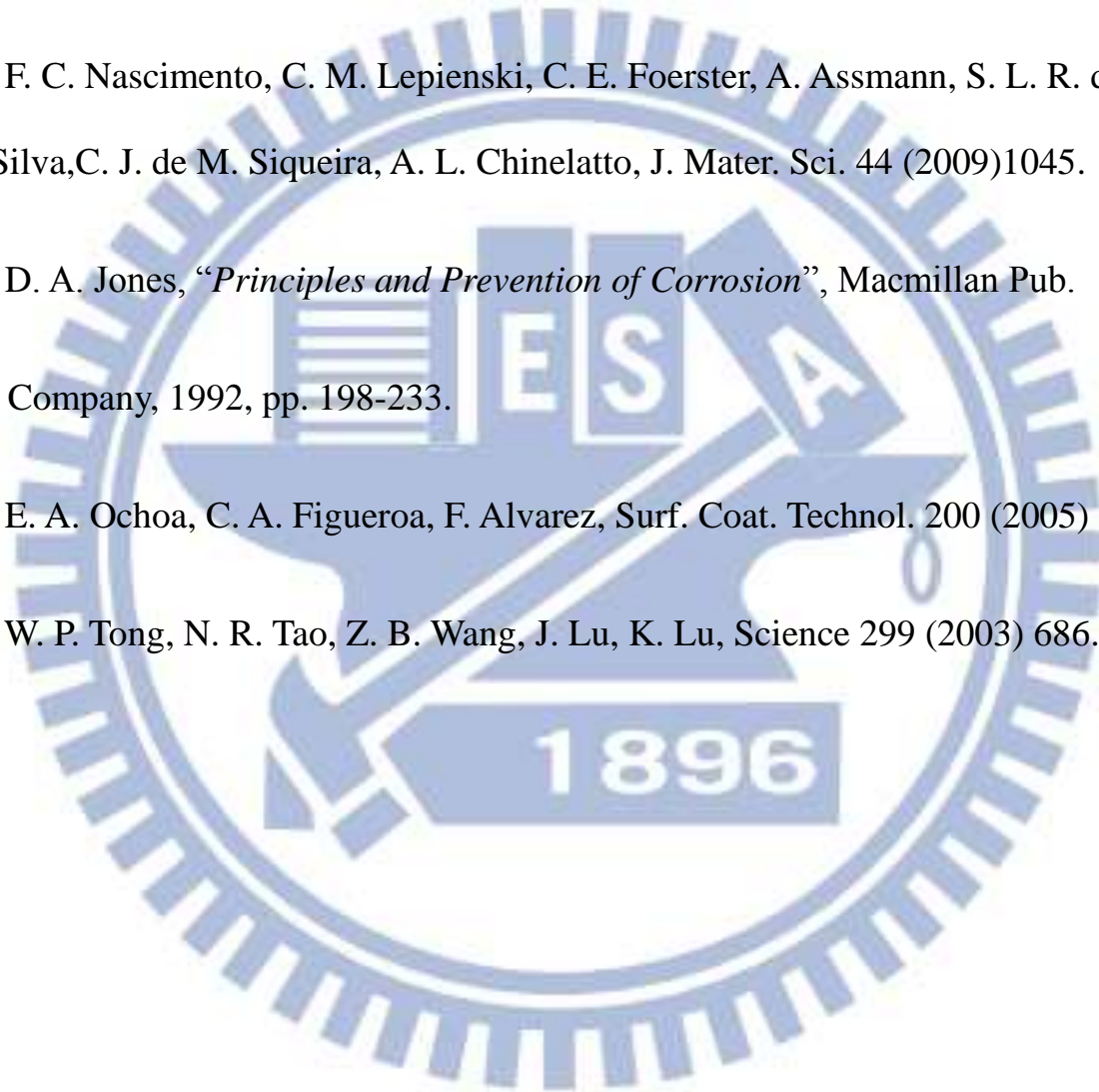
[38] A. Assmann, C. E. Foerster, F. C. Serbena, C. M. Lepienski, A. L. Chinelatto, IEEE Trans. Plasma Sci. 39 (2011) 3108.

[39] F. C. Nascimento, C. M. Lepienski, C. E. Foerster, A. Assmann, S. L. R. da Silva, C. J. de M. Siqueira, A. L. Chinelatto, J. Mater. Sci. 44 (2009) 1045.

[40] D. A. Jones, "*Principles and Prevention of Corrosion*", Macmillan Pub. Company, 1992, pp. 198-233.

[41] E. A. Ochoa, C. A. Figueroa, F. Alvarez, Surf. Coat. Technol. 200 (2005) 2165.

[42] W. P. Tong, N. R. Tao, Z. B. Wang, J. Lu, K. Lu, Science 299 (2003) 686.



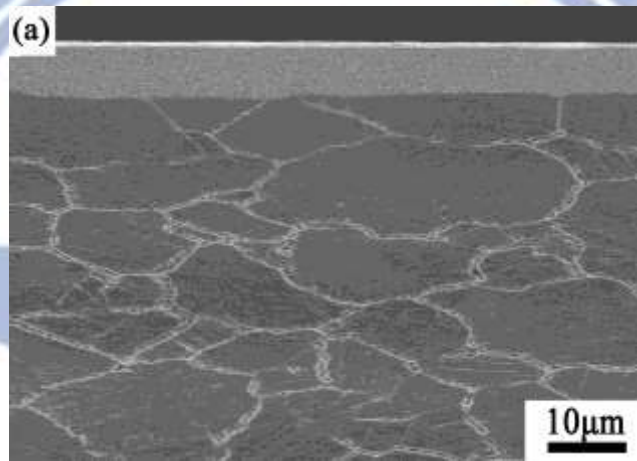


Figure 3.1(a)

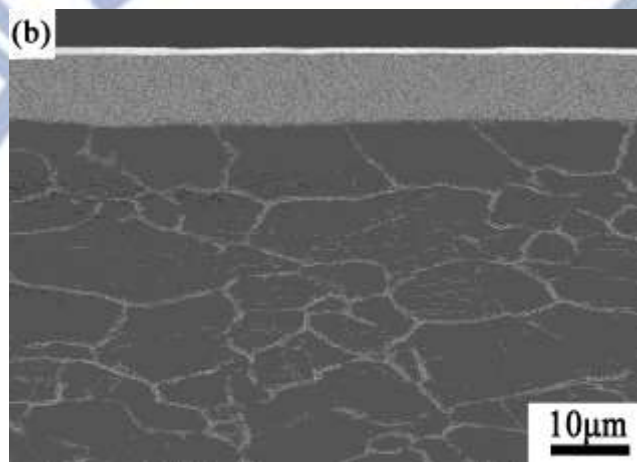


Figure 3.1(b)

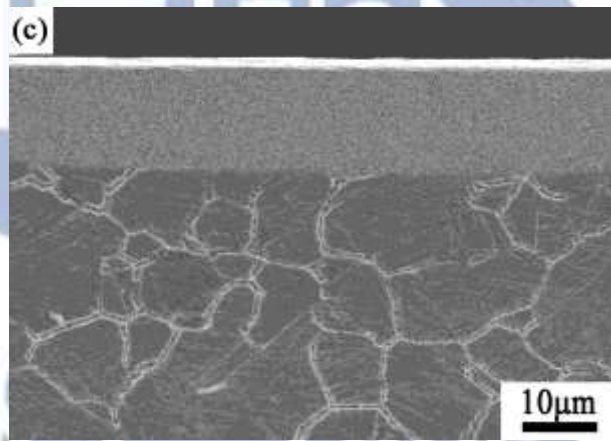


Figure 3.1(c)

Figure 3.1 SEM images of the present nitrided alloys treated with nitriding pressure of (a) 133 Pa, (b) 399 Pa, and (c) 798 Pa, respectively. (Etched in 5 % nital .)

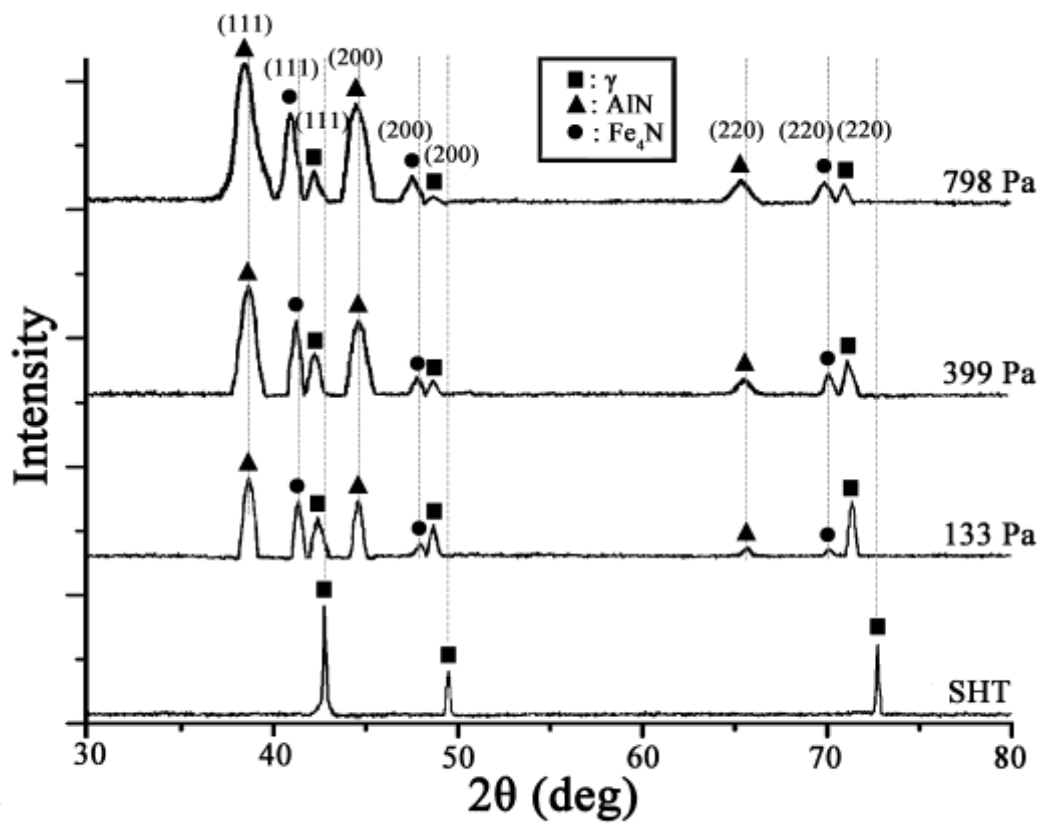


Figure 2

Figure 3.2 XRD results for the untreated and nitrided alloys.

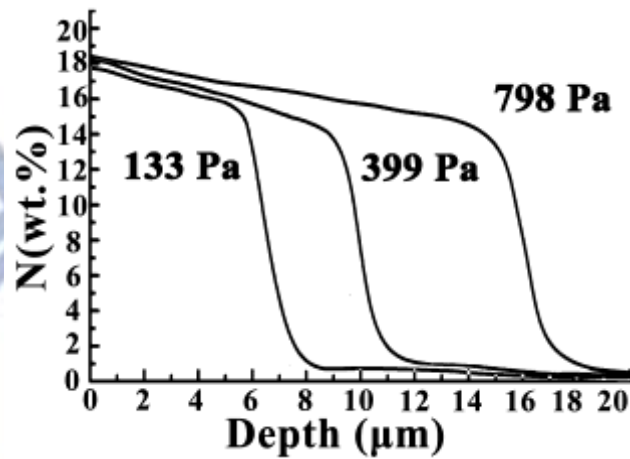


Figure 3.3 (a)

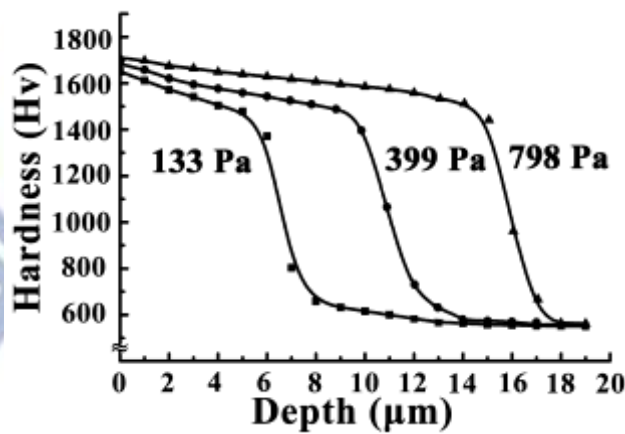


Figure 3.3 (b)

Figure 3.3 (a) Nitrogen concentration, and (b) hardness profiles as a function of the depth for the present nitrided alloys treated with nitriding pressure of 133 Pa, 399 Pa and 798Pa, respectively.

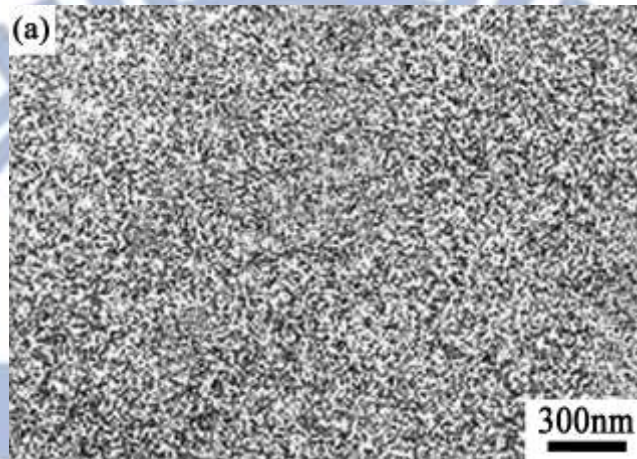


Figure 3.4 (a)

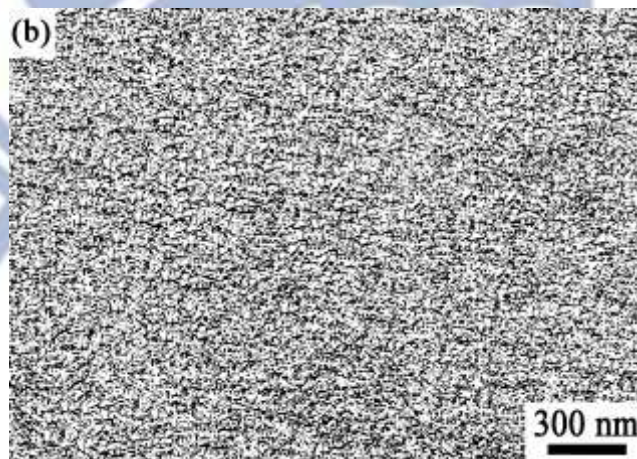


Figure 3.4 (b)

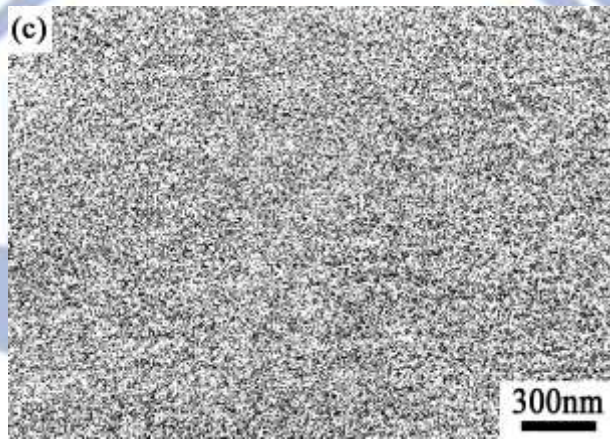


Figure 3.4 (c)

Figure 3.4 SEM images of the surface of nitrided alloys treated with nitriding pressure of (a) 133 Pa, (b) 399 Pa, and (c) 798 Pa, respectively.

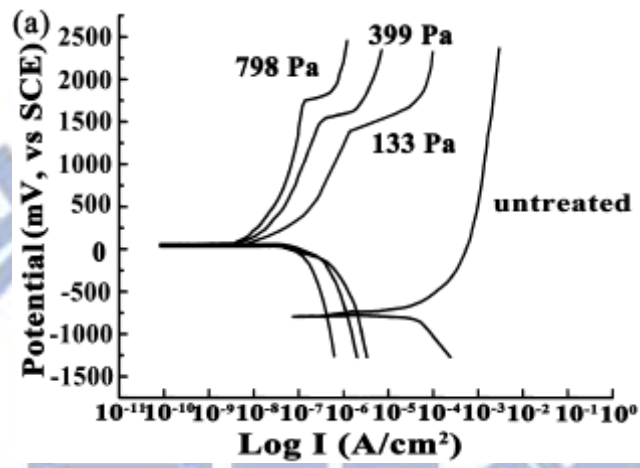


Figure 3.5 (a)

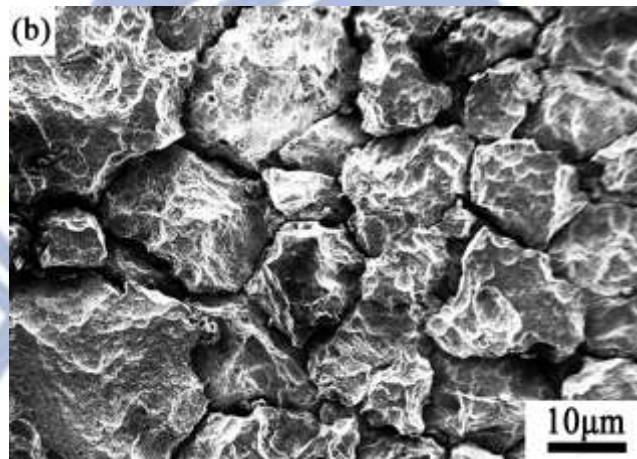


Figure 3.5 (b)

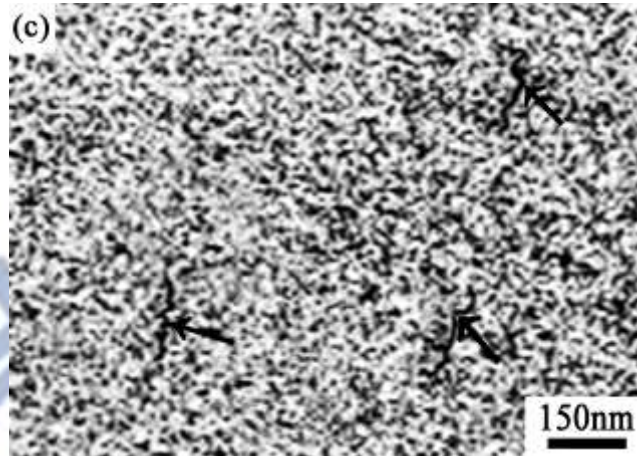


Figure 3.5 (c)

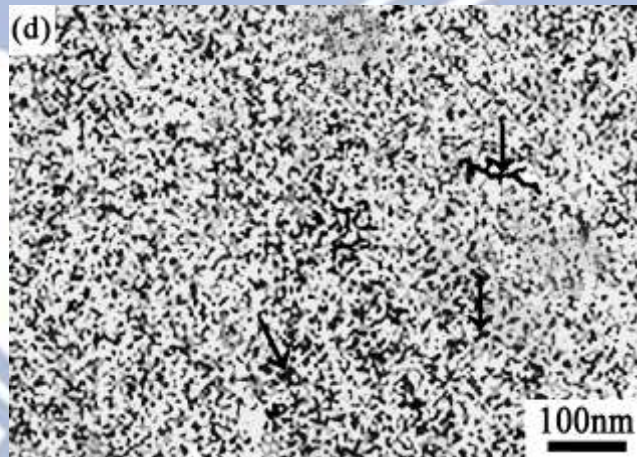


Figure 3.5 (d)

Figure 3.5 (a) Polarization curves for the untreated and nitrided alloys in 3.5% NaCl solution. (b)-(d) : SEM images of the polarized alloys, (b) untreated alloy, (c-d) nitrided alloys with nitriding pressure of 133 Pa and 798 Pa, respectively.

Table 3.1 The volume fraction and particle size of AlN phase estimated by LECO2000 image analyzer as well as the prominent corrosion resistance parameters for the SHT and nitrided alloys.

	Thickness of nitrided layer	Surface				Polarization test results in 3.5% NaCl solution				
		Volume fraction of AlN	Particle size of AlN	Hardness	Nitrogen concentration	I_{corr} (A/cm ²)	I_p (A/cm ²)	E_{corr} (mV)	E_{pit} (mV)	ΔE (mV)
SHT				545Hv		8.2×10^{-6}		-782		
133 Pa	6 μ m	71.5%	14.3nm	1641Hv	17.7wt.%	1.2×10^{-8}	2.8×10^{-6}	+30	+1360	+1330
399 Pa	9 μ m	77.1%	9.6nm	1675Hv	18.2wt.%	8.1×10^{-9}	3.5×10^{-7}	+42	+1505	+1463
798 Pa	15 μ m	80.3%	8.3nm	1710Hv	18.4wt.%	2.4×10^{-9}	2.0×10^{-7}	+58	+1765	+1692

List of Publications

● Journal Papers

1. K.M. Chang, C.G. Chao and T. F. Liu*, "Excellent combination of strength and ductility in an Fe-9Al-28Mn-1.8C alloy", Scripta Mater. 63 (2010) 162-165.
2. K. M. Chang, C. C. Kuo, Y. W. Chang, C.G. Chao, T. F. Liu*, "Effects of gas nitriding pressure on the formation of nanocrystalline AlN in plasma nitrided Fe-9Al-28Mn-1.8C alloy", accepted for publication in Surface and Coatings Technology (Jun. 2014).

● Conference Papers

1. 張凱明、陳柏至、林志龍、段逸軒、蔡國棟、劉亮延、王浩仰、朝春光、劉增豐, "鐵-9 鋁-30 錳-2 碳合金之顯微結構與機械性質", Proceedings of The 2009 Annual Conference of The Chinese Society for Materials Science.
2. 王喬立、陳柏至、王浩仰、張凱明、林志龍、段逸軒、朝春光、劉增豐, "鐵-9 鋁-30 錳-6 鉻-1.8 碳合金之顯微結構與抗腐蝕性質", Proceedings of The 2010 Annual Conference of The Chinese Society for Materials Science.
3. 王承舜、林志龍、張凱明、陳柏至、林晟毅、孔睦穎、陳思漢、朝春光、劉增豐, "鐵-8.5 鋁-30 錳-1.0 碳合金之機械性質", 台灣鑄造學會 2011